INSTITUTO TECNOLÓGICO Y DE ESTUDIOS SUPERIORES DE MONTERREY

CAMPUS MONTERREY

SCHOOL OF ENGINEERING AND SCIENCES

BIDIRECTIONAL AC ELECTROOSMOTIC PUMPING BY HYDRODYNAMIC CHANNELING USING 2D AND 3D PHOTORESIST-DERIVED CARBON MICROELECTRODES

A dissertation presented by

Matías Vázquez Piñón(Student)

Submitted to the School of Engineering and Sciences in partial fulfillment of the requirements for the degree of

Doctor of Philosophy

In

Information Technologies and Communications

Major in Microsystems

Monterrey, Nuevo León, May 20th, 2019

A mi familia...
Este esfuerzo no hubiera sido posible sin su apoyo y cariño.

Acknowledgements

I believe that in order to become a great scientist, one have to surround theirselves by great scientists, and learn something new from them every single day. On my journey of persuing a Ph.D., I was very lucky on finding myself surrounded by great scientists, whom at the same time, are also great human beings and friends; and I am really grateful of have had the chance of working with them.

First off, I thank Dr. Sergio Omar Martínez Chapa, who has conceded me his trust, guidance and friendship not only on this journey, but even before, as a professor and Master thesis advisor. I also thank Dr. Hyundoo Hwang for his support and trust. I believe we were able to make the most out of this research project through hard work and constant and valuable talks. I also thank Dr. Víctor Hugo Pérez González, who trusted in me as a researcher, and not only worked together on this project, but also on other valuable collaborations.

I also acknowledge those who always were there supporting and advising me, and always been open for collaborations. I thank Dr. Bidhan Pramanick, Dr. Sergio Camacho León, Dr. Roberto Carlos Gallo Villanueva, Dr. Arnoldo Salazar Soto, Dr. José Manuel Rodríguez Delgado, Dr. Graciano Dieck Assad, M.Sc. Braulio Cárdenas Benítez, M.Sc. Felipe Gilberto Ortega Gama, Eng. Regina Elizabeth Vargas Mejía, and, last but not least, the student Enoch Kang from KAIST University, for helping me out on those never-ending journeys of processing data from my experiments.

My research stay at University of California, Irvine, was one of the very best experiences I've had in my life. Having the opportunity of being there was a life-changing experience and I'll always remember it. I thank Dr. Marc Madou for taking me as part of his research group, and for always being there with his advice, support and great sense of humor that makes science a pleasant experience. I also thank Dr. Lawrence Kulinsky for always being interested on my professional development, and for his brilliant ideas to make the most out of our research projects.

At UCI I met very smart and friendly people that were always accessible on helping me out on everything related to the lab and research. I want to acknowledge Dr. Ling X. Kong, Dr. Sunny Holmberg, Dr. Horacio Kido, Dr. Rahul Kamath, M.Sc. Jacob Moebius, and current Ph.D. students Alexandra Perebikowsky, Ehsan Shamloo, and Maria Bauer. Thank you, guys, for your help and friendship.

I have not only gained knowledge and professional experience throughout these years, but also great friends whom know they count on me, and I know I count on them. It is true that worthy research can't be done alone, and I am very happy that all those persons I thank here, were there when I needed them. Indeed, this one has been a long and challenging journey, and I wouldn't have made it without all of you.

Last but not least, I gladly acknowledge the support of the National Counsil of Science and Technology of Mexico, CONACyT (National Scholarship program 322105 and Basic Science program CB2014-241458); the UC-Mexus partnership between CONACyT and the University of California (Collaborative grant UCM-104728, and Small grant UCM 104199); the Bio & Medical Technology Development Program of the NRF of the Korean government (MSIT (2017M3A9E2062212/2017M3A9E2062133)); and the National Science Foundation of the United States government (CMMI-1661877), for their major support on this work.

Bidirectional AC electroosmotic pumping by hydrodynamic channeling using 2D and 3D photoresist-derived carbon microelectrodes

by

Matías Vázquez Piñón

A B S T R A C T

In microfluidics, fluid movement is keystone for the correct operation of different system stages, including convective mixing, electrochemical sensing, and affinity bonding in immunoassays. Even though the most commonly developed microfluidic pumps are unidirectional, over the last decade, bidirectional approches have been developed to considerably improve the overall performance of microfluidic systems. Furthermore, the exploration of new approaches for bidirectional pumping allows the creation on fully integrated, stand-alone systems for applications including drug delivery, clinical analyses, cell culture, among many others.

AC electroomosis is a suitable electrokinetic approach for fluid driving in microchannels. Opposite to commonly-used microfluidic pumping approaches, in AC electroosmosis no moving elements are required, and only a set of electrodes is used, thus fabrication of devices is remarkably simple and cost-effective as a stand-alone pump, or for integration with other microfluidic components. In this work we propose a hydrodynamic mechanism to reverse the flow in AC electroosmotic micropumps in order to attain bidirectional pumping. The flow reversal mechanism involves the channeling of the vortices generated by electroosmotic manners, by taking advantage of the microchannel geometrical properties; particularly, the microchannel height, which is closely related to the stimulating electrodes' width and, in consequence, to the enclosed vortices' size.

We use the Carbon-MEMS fabrication process to develop two electrode architectures: asymmetric planar and high-aspect-ratio microposts. The carbonaceous material obtained from this process is characterized to validate the adecuate properties for electrokinetic applications, and the micropumps are then assembled by bonding a PDMS microchannel. The flow development by AC electroosmotic means is profoundly studied using a bidimensional finite element model comprehending the Poisson-Nernst-Plank-Navier-Stokes equation set to closely emulate the vortex formation on the electrodes surface. To explore the effect of electrode asymmetry ratio on the fluid velocity, we compare three asymmetry ratios for both, coplanar, and high-aspect-ratio architectures.

Experimental results are presented and a fluid velocity analysis is carried out for forward and reverse flows. An explanation of how flow reversal is achieved by hydrodynamic channeling is detailed, and experimental test analysis provides the conditions under flow reversal is produced, such as amplitude and frequency of the applied AC signal, and asymmetry ratio of electrodes. Furthermore, the effect of microposts on fluid velocity and flow reversal is thoroughly discussed. Hydrodynamic channeling using AC electroomosis is a new approach for bidirectional pumping, thus areas of opportinity are presented for future developments in this field, such as optimization of electrode asymmetry ratio, micropost spacing and microchannel height.

Contents

List of Figures

List of Tables

Chapter 1

Introduction

Important and exciting breakthroughs have been recently reported in scientific literature regarding diagnostics, treating and tracking several medical conditions such as cancer, diabetes and cholera, among many others [1–4]. Today, for instance, is possible to quantitatively determine if an specific treatment or set of treatments are efficiently working on a cancer patient by microfluidics analysis, in which circulating tumor cells are detected and counted in a microliter whole blood sample by means of antigen-antibody bindings [5]. This is possible due to high-tech manufacturing processes that enable the fabrication of different materials to biofuncionalize them with antigens, proteins, etc., and to finally process biological samples due to biocompatibility. Moreover, Point-of-Care (POC) assays have been also developed to be used in the poorest regions of the world, and which, at a very low cost, are used to diagnose diverse infectious diseases, including HIV a syphilis [6–8].

Commonly, clinical testing are carried out in animals with a similar system that the human body. Pigs, rats, rabbits, chimps, among others, are used as subject for different medical experiments such genetics, drug testing and toxicology tests, just to mention a few. The British Royal Society states that *"from antibiotics and insulin to blood transfusions and treatments for cancer or HIV, virtually every medical achievement in the past century has depended directly or indirectly on research on animals*[1] *"*. Thus, it is important to find approaches to conduct research considering biomedical ethics when using animals for medical trials and to reduce to the minimum the suffering of animals.

As human life style evolves, new food processes are applied to our daily diet, our cities are more polluted and living is more accelerated. Diseases become more complex and takes more time to us to find their cures. Without constant medical developments, it would be even harder for us to fight diseases or even to improve

[1] Statement of the Royal Society's position on the use of animals in research.

quality of life when cures are not yet developed. It is difficult for us to think about how our parents and older generations dealed with their communications necessities over the last decades without cellphones and internet and, it is similar if we think about medical and healthcare technologies. Thanks to that constant research, today are aware of stem cells research, HIV cocktails, targeted cancer therapies, laparoscopic surgery, Human Papillomavirus Vaccine, bionic limbs, face transplants, early detection of Parkinson's disease, and many other developments. Furthermore, today we are able to sense almost everything in our body in a non-invasive manner; something that a few years ago was difficult and expensive.

The next generation research, specially that related to diagnose and treat human conditions have to be fast enough to prevent massive human loss, low cost, efficient and reliable and without affecting other living species, and microfluidics is a convenient candidate to achieve this.

1.1 The Role of Micropumps in Microfluidics

Microfluidics is the discipline that studies the devices and methods for driving small amounts of fluids (from 10^{-9} to 10^{-18} liters) by using channels with dimensions in the scale of micrometers ($10^{-6}-10^{-4}$ meters) [9,10]. At this scale, the Reynolds number—which is the ratio of inertial forces to viscous forces, and provides the degree of *laminar* or *turbulent flow*—is given by

$$\mathrm{Re} = \frac{\rho \nu D}{\eta} \ll 1 \tag{1.1}$$

Here ρ, ν, and η are the density, velocity and viscosity of the fluid; and D is the hydraulic diameter of the particle. At low Reynolds numbers, such as those commonly found in microfluidics, viscous forces dominate over inertial forces, resulting on the observation of *laminar flow*, meaning that the fluid circulates in the form of ordered sheets [11, 12]. Microfluidics brings up important capabilities for fluid analysis, including the possibility to process samples using very low volumes of both, analytes and reagents, short processing times, low cost of analyses, and high sensitivity. Microfluidic devices have found a broad variety of applications on medical and health industries. Nowadays, it is possible to diagnose a wide variety of diseases using microfluidics implemented on Lab-on-a-Chip (LoC) or micro Total Analysis Systems (μTAS) devices, which are portable, fast and low-cost platforms used to carry out conventional laboratory analysis in a miniaturized fashion (see Figure 1.1) [13]. LoC and μTAS devices are integrated from different essential components, including microchannel networks where all the samples and reagents are processed, as well as sensors and actuators, valves and pumps, among others. Microfluidic platforms allow to investigate and develop new drugs and provide an innovative way to administer them to patients—the so called drug-delivery

systems. Environment monitoring is other widely explored application of microfluidics, where the quality of our environment is studied using biofunctionalized chips, for the detection of possible harmful substances in food and water, among other possibilities.

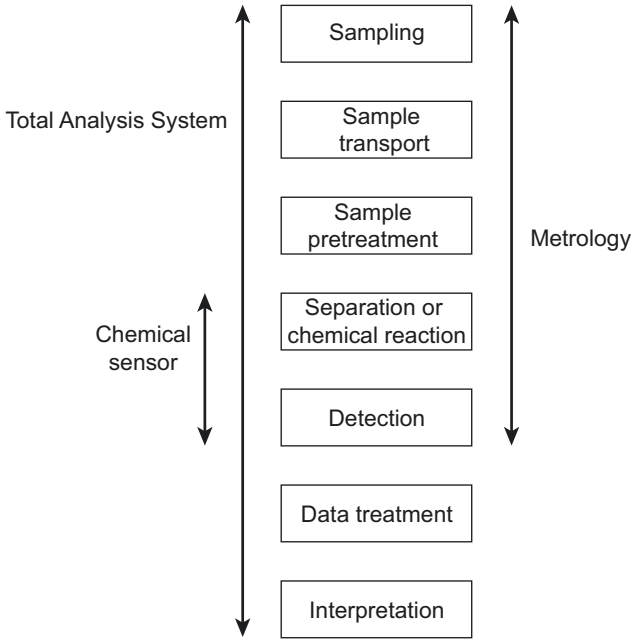

Figure 1.1: Steps of a chemical analysis in a Total Analysis System.

The increasing interest for stand-alone microfluidic analysis systems, have motivated the quest for novel fluid pumping techniques governed by low Reynolds number regimes to achieve system unification, high performance and reliability, and low fabrication and operation costs. The overall performance of a microfluidic system is highly determined by the accurate fluid driving in the microchannel networks, which provides appropriate operational conditions to other system components running concurrent tasks. This encompasses from general purpose tasks such as pumping and mixing, to extremely high-precision mechanisms, including drug delivery systems [14], low concentration electrochemical sensors, energy generation in fuel cells, and many others. In such systems, fluid transport is typically used for sample distribution in microchannel networks, reagent/sample mixing and molecular separations, among many other tasks. For this, a variety of physical phenomena is used for fluid/particle processing in microfluidics, incluidng pressure gradients, capillary effects, gravity, Lorentz forces, centrifugal forces, and electrokinetics, among others [10].

From the conception of LoC and μTAS in the early 90's, integration of different microfluidic elements into a single die has become a scientific challenge to achieve stand-alone chemical/biological analysis systems [15–17]. Particularly for fluid pumping in microchannels, several mechanisms have been developed, which include mechanical and non-mechanical approaches. On one side, mechanical micropumps are mostly

driven by diaphragm displacements complemented by other solid elements such as valves. On the other side, non-mechanical approaches make use of intrinsic properties of the fluid to generate fluid movement [18]. Non-mechanical, valveless fluid driving techniques have become convenient alternatives to their mechanical counterpart due their structural simplicity, low fabrication complexity, low cost and satisfactory performance. These techniques include the use of electric or magnetic fields [19, 20], light [21] or acoustic waves [22], as the driving principle, among others. Figure 1.2 shows the classification of micropumps according to Laser and Santiago, 2004 [18].

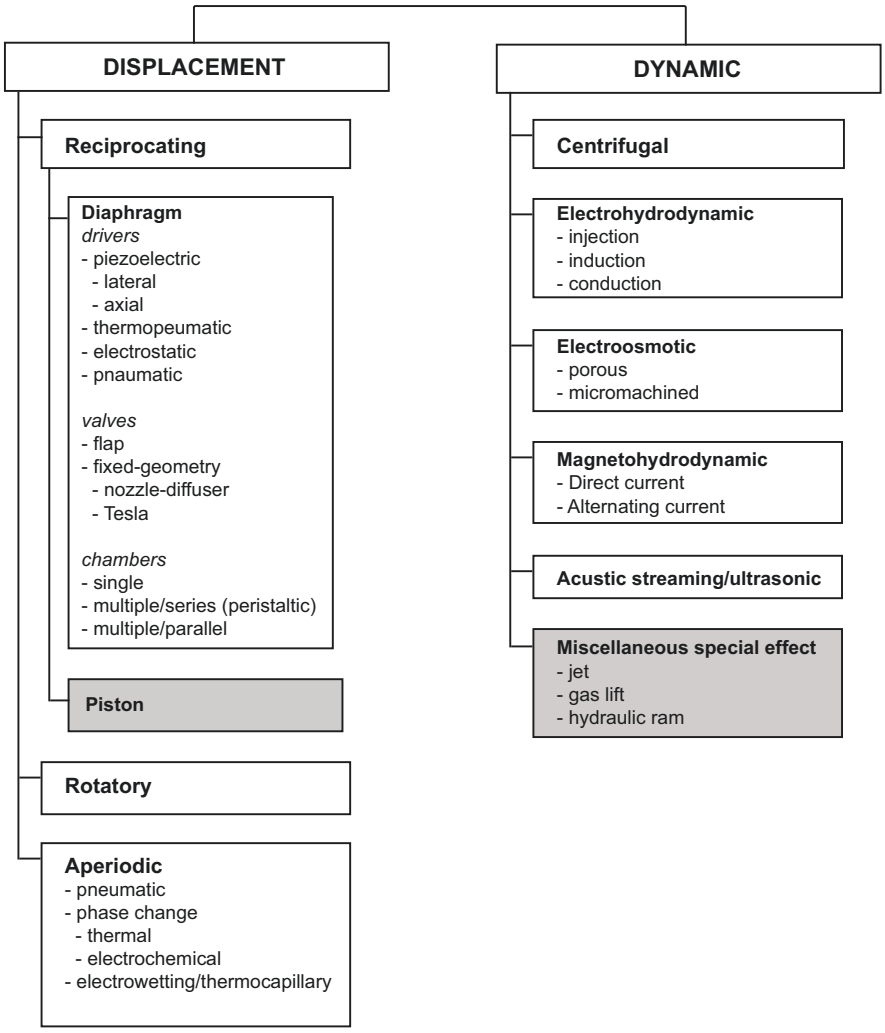

Figure 1.2: Classification of micropumps.

From Figure 1.2, displacement micropumps make use of pressure forces generated by a physical moving actuator on a volume of fluid. These systems mostly include piezoelectric [23], pneumatic [24] and electrostatic [25] micropumps. However, fabrication of these devices often requires complex and expensive micromachining processes, and there is an inherent propensity for mechanical wearing, fatigue, and clogging that might limit

the micropump throughput and cause premature failure.

To overcome limitations of displacement mechanisms, pumping techniques with no moving parts have been successfully implemented in microfluidic systems, which are referred to as dynamic micropumps. Here, various types of transmitters continuously transfer non-mechanical energy directly to the fluid to generate momentum. The most extensively studied dynamic approaches include thermal [26], electrohydrodynamic (EHD) [27], magnetohydrodynamic (MHD) [28], and DC and AC electroosmotic micropumps [29,30]. In this case, the lack of moving parts significantly simplifies the micropump structural framework, generally leading to a straightforward and cost-effective device fabrication process. EHD and DC electroosmosis (DCEO) pumping approaches have been studied extensively; however, the extremely high operational voltages affect the electrical properties of the fluid and require bulky external power generators [31]. Moreover, for MHD pumping the use of external magnets/electromagnets is required [32], which limits the ability to integrate all the elements into a single portable device.

From the dynamic standpoint, it has been recognized that AC electroosmosis (ACEO) has the advantage of low structural complexity (commonly constituted only by an electrode array encompassed in a microchannel). Also, due to its direct and localized actuation, ACEO allows the development of independent fluid control mechanisms at different microchannel locations, and at different phases of the analysis process [33–37]. In ACEO, a low-amplitude (1–10 V_{PP}), low-frequency (10 Hz–100 kHz) AC signal is applied across electrode pairs separated by a few micrometers gap to induce a strong, non-uniform electric field that propels ions in the fluid adjoining the electrodes [38]. Movement of these ions and their hydrated shells is transferred to the surrounding fluid by viscous forces [39]. In order to cause net flow (and not just re-circulation above the electrodes), asymmetry in the electrodes geometry is introduced by having a narrow electrode E_N paired with a wider electrode, EW. In this work, the term forward flow indicates the net flow of the fluid from E_N towards E_N.

Unidirectional fluid pumping is the most commonly used approach in microfluidics, and it has been successfully implemented is most of the applications where fluid convection is required. To increase efficiency of the overall system in applications carrying out tasks as biochemical sensing, particle separation, and in general microfluid processing systems, bidirectional fluid driving is desirable to increasing the interaction of molecules of interest and surfaces and/or to achieve better fluid distribution across complex microchannel networks.

Bidirectional flow is typically achieved by commercially-available macroscale mechanical pumps—*i.e.* the use moving elements to produce fluid momentum—such as syringe pumps, peristaltic pumps or even manual pipetting. However, operation of large-scale mechanisms in microfluidic applications is not only cumbersome

to drive micro/nanoliter volumes; also, the use of large-scale devices restrains from system integration and portability, which are essential characteristics for stand-alone devices. However, microscale mechanical techniques for bidirectional pumping have been more recently developed for portability purposes, and have been successfully implemented in microfluidic systems. Table 1.1 summarizes in chronological order, the most relevant developments on bidirectional micropumps over the last decade, particularly describing their actuation mechanism and microchannel materials. The highlighted row corresponds to this work.

Table 1.1: Relevant publications on bidirectional microfluidic pumps, part 1.

Year	Mechanism	Classification	Valve type	Channel	Media
2006 [40]	Piezoelectric	Displacement	Active	Silicon	Water
2010 [41]	Piezoelectric	Displacement	Valveless	PDMS	Ethanol
2011 [42]	Piezoelectric	Displacement	Passive	PMMA/SU-8	Water
2011 [43]	Piezoelectric	Displacement	Active	Silicon	Water
2013 [44]	Piezoelectric	Displacement	Active	Polymeric	Water
2013 [45]	Electromagnetic	Displacement	Valveless	PDMS	Water
2015 [46]	Perisaltic	Displacement	Valveless	Polyimide	Gas
2016 [47]	Piezoelectric	Displacement	Valveless	PMMA	Water
2018 [48]	Electromagnetic	Dynamic	Valveless	PDMS	Water
2018 [49]	Electromagnetic	Displacement	Valveless	Aluminum	Water
2019 [50]	AC Electroosmosis	Dynamic	Valveless	PDMS	Water

Then, Table 1.2 details on the flow rates achieved in those corresponding publications from Table 1.1, as well as the operating conditions and fabrication techniques.

Table 1.2: Relevant publications on bidirectional microfluidic pumps, part 2.

Ref	Forward flowrate	Backward flowrate	Operating condition	Fabrication method
[40]	1.4 ml/min	1.4 ml/min	4.2 V @ 17 Hz	CVD/photolithography/RIE
[41]	20.94 µl/min	20.94 µl/min	220 V @ 45–300 Hz	Soft-lithography
[42]	16.4 ml/min	5.1 ml/min	150 V @ 355 Hz	Machining/photolithography
[43]	1.64 ml/min	1.65 ml/min	45 V @ 30 Hz	Silicon micromachining
[44]	4.8 ml/min	4.8 ml/min	±260 V	Hot embossing
[45]	1.52 ml/min	1.48 ml/min	1–20 Hz	Soft-lithography
[46]	136 µl/min	136 µl/min	60 V & 120 V @ 15 Hz	Photolithography/DRIE
[47]	0.4 ml/min	0.4 ml/min	500–800 V @ 10 Hz	Precision machining
[48]	67.2 µl/min	67.2 µl/min	1.4 V @ 9 Hz	Soft-lithography
[49]	37 ml/min	37 ml/min	1.6–2 A @ 3.3 Hz	Precision machining
[50]	0.091 µl/min	1.014 µl/min	2–20 V @ 1–200 kHz	Photolithography

As can be seen from Table 1.1, displacement micropumps for bidirectional fluid driving are the most commonly developed over the last decade, and the dynamic devices have been developed using only electromagnetic and AC electroosmotic mechanisms. A clear trend on discarding the use of valves in micropumps

can also be observed. Then, from Table 1.2, the most noticeable limitation of the dynamic mechanisms for bidirectional pumping is the low forward and backward flow rates, compared to displacement mechanisms; and for the particular case of the present work, asymmetric flow rates between forward and backward directions. However, fabrication methods are simpler for dynamic mechanism, as well as very low power consumption, as can be deduced from the operating conditions column.

Even though ACEO is commonly employed as a unidirectional pumping mechanism, in this work we take advantage of the geometry of the microchannel enclosing the fluid to hydrodynamically reverse the net flow direction (i.e. force the net flow from E_{W} towards E_{N}). That is, we take advantage of the geometrical characteristics of the microchannel enclosing the fluid to force the flow to reverse by preventing the vortices to complete a swirl in the direction of the forward flow. ACEO micropumps are able to control the fluid rate of a bulk analyte by varying the applied voltage signal parameters (amplitude, frequency, and phase in some cases), thus avoiding the use of moving parts, prevent analyte warming, and reduce undesired chemical reactions.

In the present work is reported the development of bidirectional ACEO pumping by means of hydrodynamic channeling of fluid streamlines contained in a microfluidic channel. Here, we take advantage of the wide electrochemical stability of GC to develop asymmetric coplanar and high-aspect-ratio microelectrodes to form bidirectional micropumps. In this sense, asymmetric coplanar electrodes were fabricated using the Carbon-MEMS technique, which consist of photolithographic patterning and pyrolysis. Alongside, microposts were developed atop the planar structure using a second photolithography step to determine the effect of high-aspect-ratio structures on the overall fluid velocity and direction. The resulting glassy carbon material was characterized to determine its intrinsic properties by Raman and energy-dispersive X-ray (EDX) spectroscopies. This, to confirm that the electrode material properties (composition and graphitic/amorphous carbon content) are appropriate for utilization of these electrodes for electrokinetic applications. Visual inspection was also carried out SEM and Confocal microscopies to determine the morphological characteristics of the electrodes. A finite element model was developed to show the flow development as a result of the applied potential to the acting electrodes. Finally, experimental tests were carried out and fluid velocities in reverse and forward directions were computed for both, coplanar and HAR structures, and the results were analyzed and discussed.

1.2 Thesis Outline

Chapter 2 of this work provides a solid theoretical background on electrohydrodynamics including a detailed electric double layer description, the electroosmotic phenomenon and the principle of fluid pumping by AC electroosmosis. **Chapter 3** describes the Finite Element analysis that was carried out to study the flow development by ACEO means. **Chapter 4** details the fabrication process of asymmetric coplanar and high-aspect-ratio electrode arrays using the Carbon-MEMS fabrication process. In **Chapter 5**, experimental results on the effect of the electrodes architecture are presented, including fluid velocities and flow reversal conditions. Finally, in **Chapter 6**, concluding remarks on the presented work, as well as future works is given.

Chapter 2

Non-linear electrokinetic phenomena

The observation of a frequency-dependent fluid movement during a dielectrophoretic particle manipulation experiment, gave rise to a new reseach field in electrokinetics[1]. The scientists who discovered and explained this phenomenon named it *AC electroosmosis* [39]. Electroosmosis is defined as the relative movement of a fluid with respect to a solid charged or conductive surface as a result of an applied electric field gradient.

In ACEO pumping, electrode arrays are placed on the channel walls very close to each other (usually a few microns) to generate a strong electric field using low amplitudes ($< 10\,V_{PP}$) and frequencies (1-100 kHz), to induce an electric double layer (EDL) at the interface between the electrode and solution. The effect on the electrode/gap and electrode/electrode ratios, as well as the fluid direction and velocity due to the signal and microchannel characteristics have been previously verified by simulation [51], and experimentally [52,53]. However, a fully developed methodology for the fabrication of ACEO micropumps based on the required flow characteristics and integration in LoC systems has not been formally developed yet. ACEO micropumps are versatile enough to drive fluids from nanoliters to the microliters by applying low-amplitude AC potentials. ACEO has been successfully implemented to drive fluids in biotechnology and medicine microsystems, such as DNA concentrators and amplifiers [34,37], cellular analyzers [54], immunoassays [36], and chromatography [55], among others.

This fluid movement was found to be strongly dependent on the fluid's electric conductivity, which is directly related to the amount of free electric charges conforming the EDL at the interface between the fluid and the acting electrodes. During the alternance from a positive to negative cycle of the applied AC signal—or viceversa—the electric charges conforming the EDL relax and try to reach electrostatic equilibrium as in the bulk fluid, where the electric field has no significant influence, due to the switching on direction of the

[1]The first study reporting electroomosis was published in 1809 by F. F. Reuss in the *Proceedings of the Imperial Society of Naturalists of Moscow*

electric field. Under this basis, it was then determined that the observed fluid movement only occurred for frequecies below the relaxation time of the charges during the AC signal alternance.

Viscous forces play an important role to determine new applications of AC electroomosis. Due to low Raynold numbers found in microfluidics, diffusion-dependent fluid mixing is commonly slow. Local convection due to AC electroosmotic flow has been proven to be an efficient solution for fast fluid mixing in microchannels. Due to viscous forces dragging not only fluid molecules but also bigger bodies such as other molecules, cells and particles, AC electroosmosis has also been used to drive such bodies on a controlled basis.

In order to produce ACEO bidirectional micropumps, a wide electrochemical stability of electrode materials is essential to guarantee optimal performance without electrode degradation and bubble formation. The Carbon-MEMS (C-MEMS) process have shown to be a potential candidate to fabricate cost-effective glassy carbon (GC) electrodes [56]. In this process, a photolithographically-patterned organic precursor is reduced to GC at 900°C in an oxygen-free environment [57]. The C-MEMS process for GC electrode fabrication has been successfully implemented for ACEO pumping [58], bio-sensing [59], energy generation [60] and energy storage [47], among others.

2.1 EDL-driven electrokinetics

Electroosmotic flow (EOF) is the electrokinetic phenomenon related to the movement of fluid caused by the stimulation of mobile electric charges suspended in a solution. By means of viscous forces, the movement of electric charges in the form of ions drag fluid molecules, thus forging a velocity field along the solution in the direction of the moving charges. This movement is drawn by the electric double layer (EDL) formation that arises at the interface between a solid surface and the solution containing the free charges. The EDL is created due to electrostatic interactions between ions forming the outward layer of the solid and the neighboring mobile counter-ions in the fluid. The EOF is thus strongly related to the characteristics of the EDL such as the Debye length and electric field distribution. Figure 1 depicts the constitution of the EDL.

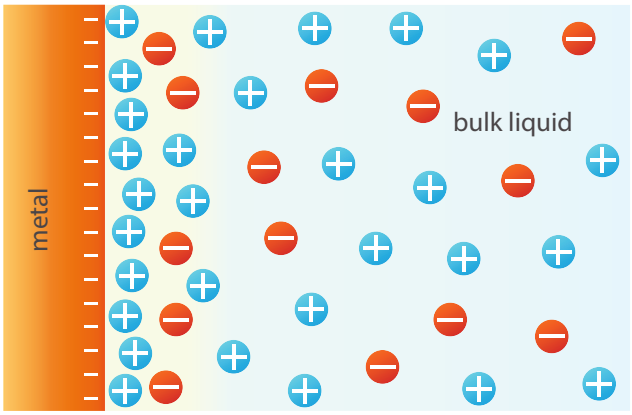

Figure 2.1: Gouy-Chapman model of the Electric Double Layer

To take advantage of this phenomenon, the EDL characteristics have to be intentionally controlled. This is accomplished by modifying its thickness by impelling an electric field into the bulk fluid by means of an external electric potential through conductive media. Typically, metallic electrodes are used to attain this task [38], but more recently, other materials have showed good results, such as glassy carbon [58], and liquid metal electrodes [30]. The shape and size of the interface between the conductive structure and the electrolyte play an important role on the control of the EDL. With the correct design and implementation of the solid/liquid interfaces, EOF can be effectively employed to perform specific tasks in Lab-on-a-Chip systems such as pumping and convective mixing.

For this purpose, DC and AC potentials can be employed to induce the electric field across the electrolyte. In DC electroosmostic flow (DC-EOF), high potentials ($\sim$500 V) are longitudinally applied across the fluid. In response to this, an electric field is induced thus impelling the free charges to move along the field direction. Figure 2.2(a) shows the typical DC-EOF setup. The zeta potential is a measure of the electroosmotic mobility in volts. The slip velocity is given by the Helmholtz-Smoluchowski equation

$$u_s = -\frac{\varepsilon\zeta}{\eta}\mathbf{E}_t \tag{2.1}$$

where $\mathbf{E}_t$ is the tangential electric field outside the EDL; ε and η are the permittivity and viscosity of the electrolyte, respectively; and ζ is the zeta potential.

Alternatively, in AC electroosmotic flow (AC-EOF), low potentials are required ($\sim 1-20$ V) since the electrodes are placed in the channel walls and commonly close enough together, and alternating signals are used to establish the flow direction. Figure 2.2(b) depicts the typical setup for AC electroosmotic flow. With this setup, the alternating field generates eddies that propels the bulk fluid with a net flow across the microchannel. For the case of AC-EOC, the fluid velocity is given by the time-averaged electroosmotic

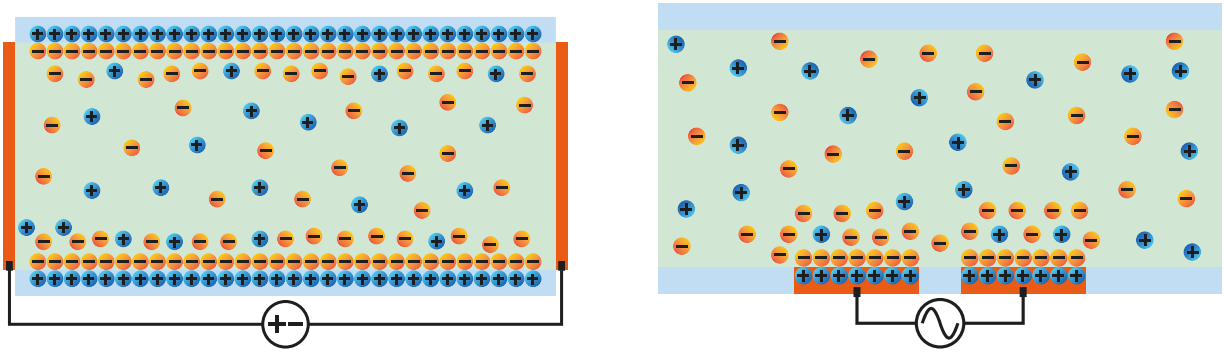

(a) AC electroosmotic flow

(b) DC electroosmotic flow

Figure 2.2: a) DC Electroosmotic Flow and b) AC Electroosmotic Flow (EDL in walls omitted in this figure).

velocity equation:

$$\langle \nu \rangle = \frac{\varepsilon V_0^2 \Omega^2}{8\eta x \left(1+\Omega^2\right)^2} \tag{2.2}$$

where $\varepsilon = \varepsilon_r \varepsilon_0$ and η are the permittivity and viscosity of the fluid, respectively; V_0 is the applied potential; x is the characteristic electrode separation (i.e., distance from the center of the gap between the electrodes to the inner electrode boundary), and Ω is the non-dimensional frequency, given by

$$\Omega = \omega x \frac{\pi}{2} \frac{\varepsilon}{\sigma} \kappa \tag{2.3}$$

where ω is the angular frequency of the established electric field, σ is the fluid conductivity, and κ is the reciprocal of the Debye length at the EDL:

$$\frac{1}{\kappa} = \lambda_D = \sqrt{\frac{\varepsilon k_B T}{2F^2 z^2 c_i}} \tag{2.4}$$

Here, k_B is the Boltzmann's constant, T is the fluid absolute temperature, F is the Faraday's constant, z is the valence of ions, and c_i is the ionic concentration of the ith species.

Both DC- and AC-EOF are used to move fluids in the micro- and nano-scales, but the later has shown to be easier to integrate into microfluidic systems because it requires lower operating voltages and electrodes are easier to pattern on subtracts by means of photolithography. Additionally, AC-driven micropumps are straightforward to change from a fluid mixing mode to fluid transport mode, or to adjust the flow magnitude or to invert the flow direction.

AC-EOF offers certain advantages over other approaches for microfluidic pumping and mixing. The foremost is the possibility of driving fluids without the need of mobile components within the microchannel.

With this, some desirable benefits can be emphasized such as low cost and simplicity of fabrication, possibility of integration with other microdevices, and the ability to drive highly programmable flows at low electric potentials, thus low power consumption [61, 62].

2.2 Hydrodynamic channeling for flow reversal

Asymmetric-coplanar IDEAs are commonly used to generate ACEO flow in microchannels by capacitive electrode polarization. Figure 1(a) shows the electric field distribution, $\mathbf{E}$, when an AC potential is applied across one pair of interdigitated electrodes. Here, the perpendicular component of the electric field, $\mathbf{E}_p$, draws neighboring opposite-charge ions suspended in the fluid towards the electrodes surface, establishing an induced EDL; whereas its tangential component, $\mathbf{E}_t$, induces a force, $\mathbf{F}$, that dispels such charges away from the gap between the electrode pair across the diffuse layer of the EDL. Switching electrode polarization draws opposite charges every half-cycle of the AC signal in the same direction [63]. The ionic displacement caused by the momentum transfer from the electrodes to the neighboring charges, allows the development of vortices above the electrodes by viscous forces exerted on the fluid molecules. These vortices sustain their flow direction even though the polarizing signal alternates from positive to negative or vice versa, since the drawn charges from the bulk fluid also alternate to satisfy electrostatic attraction forces. The size of vortices is proportional to the electrode width; thus, the electrode asymmetry ratio establishes a net flow in the direction from the weak vortex over E_{N} (narrow electrode), towards the dominant vortex over E_{W} (wide electrode).

However, the net flow direction is not only electrostatically determined by the polarization of asymmetric electrodes. Hydrodynamically, the microchannel enclosing the fluid plays a critical role for establishing flow reversal when the dominating vortex streamlines reach the top of the channel. In the forward direction (*i.e.*, flowing from E_{N} towards E_{W}), the dominating vortex establishes the flow direction by dragging fluid molecules neighboring the electrode surface as presented schematically in figure 1(b). As the size of the dominant vortex increases (with an increase in the AC amplitude), it eventually reaches the top of the microchannel. At this point, a stagnation (or transition) point is reached, where no net flow is observed, as shown in figure 1(c), when the forward flow initiated at the bottom of the fluidic channel is completely offset by the reversed flow at the top of the channel. Further increase in the dominant vortex size causes flow reversal by affecting larger mass transport at the top of the fluidic channel compared to the smaller (forward) flow at the surface of the electrode E_{W}, as seen in figure 1(d).

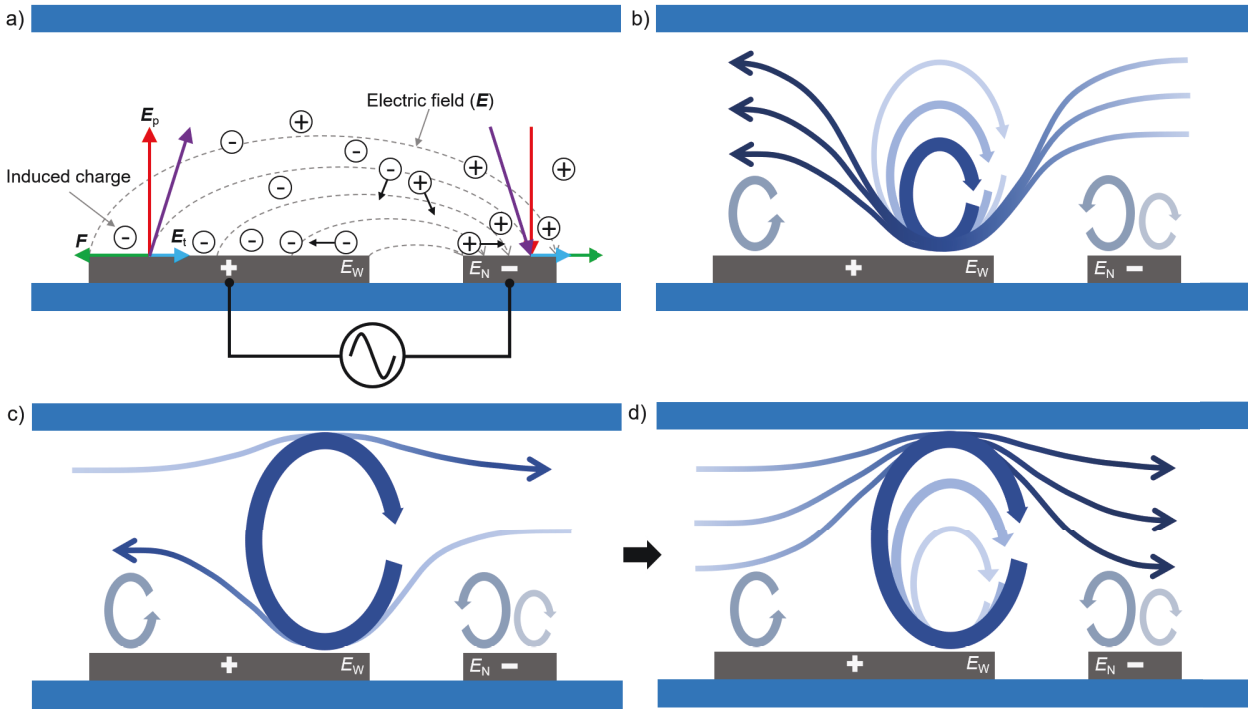

Figure 2.3: Development of fluid flow by AC electroosmosis with asymmetric coplanar microelectrodes: (a) electric field distribution and induced EDL formation, (b) forward flow generated at the electrodes surface, (c) transition point where flow generated at electrodes' surface is offset completely by development of the reversed flow at the top of the channel, and (d) reverse flow generated at the top of the channel dominating mass transport at high AC amplitudes.

Chapter 3

Numerical analysis of induced-charge ACEO flow development

A 2D finite element analysis was carried out using COMSOL Multiphysics (COMSOL, Inc., Stockholm, SE) in a two-stage study. First, a qualitative study and comparison of three different micropumps based on AC electroosmosis was carried out. It is know that these devices are capable of reaching flows in the range of commercially available pumps for microfluidic/nanofluidic applications. The micropumps are powered by a single pair of electrodes with characteristic geometries. The three most commonly used electrode geonetries, which are the asymmetric coplanar, traveling wave, and 3D or non-planar arrays), were modeled and contrasted. The Finite Element analysis was employed to characterize the three mentioned arrays under similar conditions. The mathematical model, consisting on the Poisson-Nernst-Planck-Navier-Stokes equations, has been previously applied for modeling both, micropumps [64, 65] and mixers [66], but no comparison between the mentioned electrode geometries for AC electroosmotic micropumps has bee reported yet. On this stage of the finite element analysis, the numerical model was implemented to compare the three different electrode geometries and their effect on pumping performance in microchannels. Operational requirements and qualitative results on the net flow of the described electrode geometries are reported.

The second stage of the study was used to analyze the transient flow evolution and the vortex formation during AC electroosmosis. A model that included the periodic section of the coplanar electrode array with an asymmetry ratio of 60 μm:20 μm was used to study the forward mass transport in the system. Flow reversal was not considered in this model. Furthermore, electrothermal effects were also neglected since these are usually relevant at higher working frequencies and larger fluid conductivities. The numerical model

utilizes the Poisson equation to find the electric field distribution across a pair of opposite electrodes, **E**; the Nernst-Plank equation is used to determine the charge concentration at the electrodes surface as function of **E** conprising the sum of the diffusive, convective, and electro-migration flux intensities of the ionic components. Finally, the Navier-Stokes and continuity equations are employed to establish the fluid velocity and pressure distributions in the system [35]. The electric field across the bulk fluid is given by

$$\mathbf{E} = -\nabla\varphi \tag{3.1}$$

where φ is the potential difference across the electrode pair. The Poisson equation relates **E** and the volumetric charge density across the electrolyte:

$$\nabla \cdot (-\varepsilon\nabla\varphi) = \rho_e \tag{3.2}$$

Here, $\varepsilon = \varepsilon_0\varepsilon_r$ is the relative permittivity of the medium where ε_0 is the permittivity of vacuum and ε_r is the dielectric constant of the medium. For a symmetric electrolyte (1:1), the electric charge density is given by

$$\rho_e = F\left(c^+ - c^-\right) \tag{3.3}$$

where $F = 9.6485 \times 10^4$ C/mol is the Faraday's constant, and c^+ and c^- are the positive and negative ionic concentrations in the fluid, respectively, which are determined by the molar balances:

$$\frac{\partial c_i}{\partial t} = -\nabla \cdot \mathbf{J}_i \tag{3.4}$$

Subscript i represents either of the two species; u is the velocity field, and Ji is the ionic flux for the ith species. The Nernst-Plank equation gives the ionic flux:

$$\mathbf{J}_i = \mathbf{u}c_i - D_i\nabla c_i - \frac{z_i D_i F c_i}{RT}\nabla\varphi \tag{3.5}$$

where D_i is the diffusion coefficient, **u** is the velocity field and z_i is the ion valence of each species; R is the gas constant and T is the fluid temperature. Finally, the velocity and pressure fields for an incompressible, Newtonian fluid across the fluid are described by the Navier-Stokes equation:

$$\rho\left(\frac{\partial \mathbf{u}}{\partial t} + (\mathbf{u}\cdot\nabla)\,\mathbf{u}\right) = -\nabla p + \mu\nabla^2\mathbf{u} + \rho_e\nabla\varphi \tag{3.6}$$

$$\nabla \cdot \mathbf{u} = 0 \tag{3.7}$$

where ρ, p and μ are the density, pressure and the dynamic viscosity of the fluid, respectively.

The parameters used in the developed numerical model are described in Table 3.1.

Table 3.1: Model parameters for finite element analysis.

Parameter	Value	Description
T	293.15 K	Fluid temperature
F	96,485 C/mol	Faraday Constant
Z_p	1	Ionic valence of the positive species
Z_n	-1	Ionic valence of the negative species
C_0	0.0055 mol/m^3	Initial ionic concentration
D	1×10^{-9} m^2/s	Ionic diffusion coefficient
R	8.314472	Molar gas constant
ε_0	8.85418×10^{-12} F/m	Permittivity of free space
ε_r	78.4973	Dielectric constant of water
ρ	1000 kg/m^3	Fluid density
μ	1002×10^{-3} Pa $\cdot$ s	Fluid dynamic viscosity
charge_dens	$(c_1 - c_2)F$	Electric charge density

3.1 Qualitative fluid velocity comparison between different electrode geometries

The geometries of the three electrode arrays are depicted in Figure 3.1. These electrodes are defined as boundary conditions, thus no resistive losses are considered. For a precise comparison on the performance of the micropumps, the microchannel dimensions were standardized to a transversal section of 30 μm by 10 μm, and variations were only made on the electrode geometries. Inside the microchannel, the three electrode sets were fit into a total length of 15 μm, which is distributed in the two inner quarters of the total channel width. For simplicity, the gravity effects are neglected from the results and the electrolyte is defined as an incompressible Newtonian fluid with constant relative permittivity, viscosity, density, and ionic diffusivities.

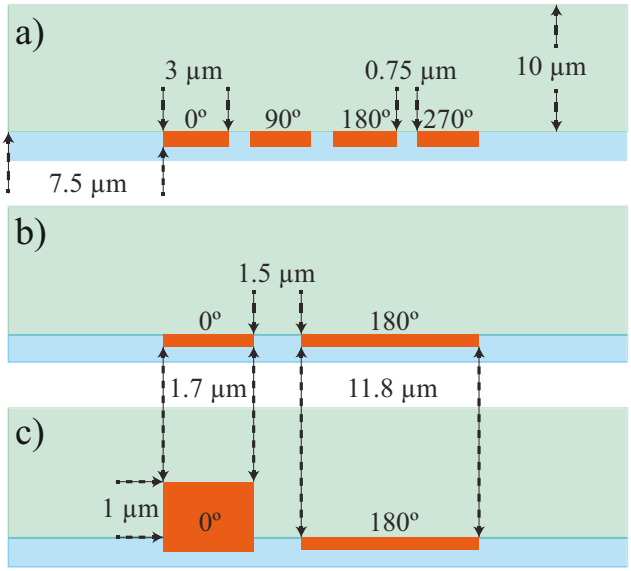

Figure 3.1: Electrode arrays: a) traveling wave, b) asymmetric coplanar, and c) 3D or non-planar.

For the traveling wave array, a set of four symmetric electrodes was used and four different phases where applied to the electrodes, $\phi = A\sin(2\pi ft + \theta)$, where θ takes value of 0, $\pi/2$, $3\pi/2$ and 2π for each subsequent electrode, as shown in Figure 3.1. For the cases of the asymmetric co-planar and 3D array, the geometries share the same electrodes and gaps lengths, and the only difference is the height of the short electrode, which is 1 µm for the 3D array. Furthermore, similar signals were applied to the electrodes with similar lengths in both cases. For the three cases of electrode arrays, a sinusoidal signal of 1 V amplitude with a frequency of 1000 Hz was used as stimulation signal.

The structure of each micropump was modeled as a bi-dimensional geometry. The non-equilibrium approach was implemented using three interfaces: the *Electrostatics* branch to solve the Poisson equation for the definition of the electric field distribution, the *Transport of Diluted Species* branch to solve the Nernst-Planck equation, and the *Creeping Flow* branch, which solves for the Navier-Stokes and continuity equations. Pertinent boundary conditions were established at liquid-solid interfaces and open boundaries were defined at the fluid inlet/outlet boundaries.

With the conditions described, vortexes are observed near the electrodes edges, as shown in Figure 3.2; and have different sizes due to the difference in the electrodes geometries: large vortexes above the large electrode and small ones above the small electrode. Due to this effect, a net flow is propelled on the bulk fluid with a net flow across the microchannel.

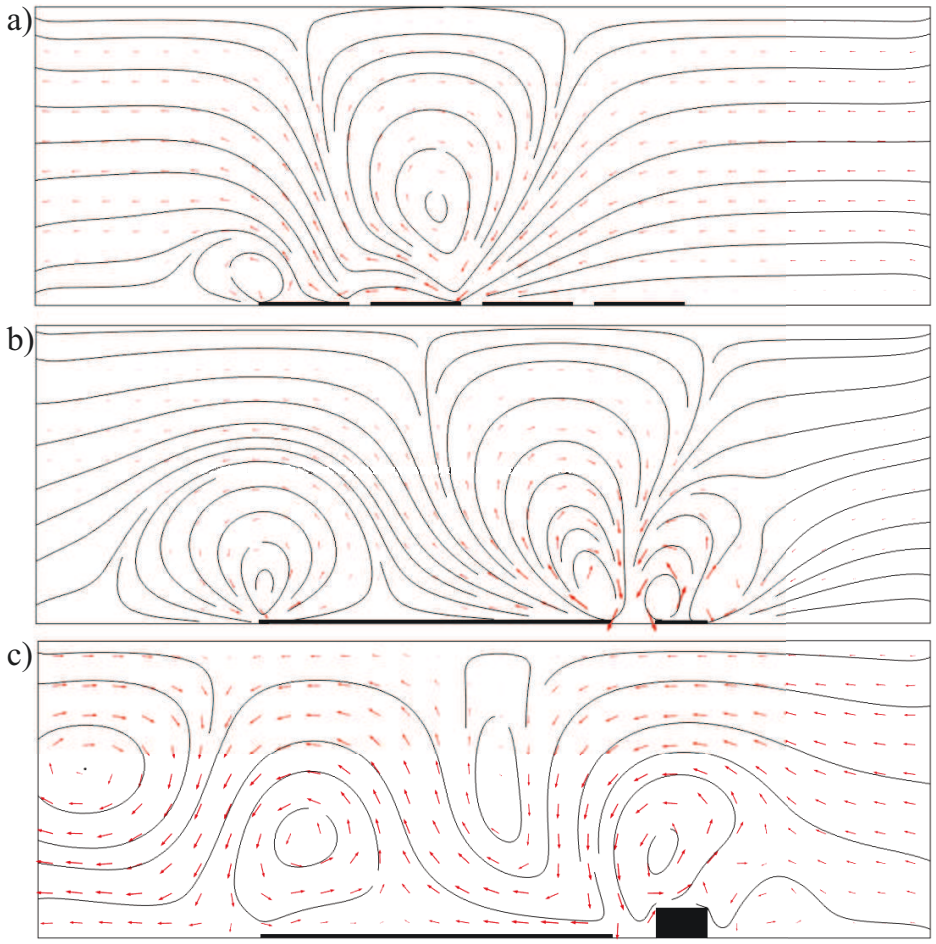

Figure 3.2: Velocity fields of the electrodes: a) traveling wave, b) asymmetric coplanar, and c) 3D.

There is a considerable increase in flow for the 3D array because the elevated electrode is blocking the back-flow generated while the electrode has a positive potential. From Figure 3.3, flow variations are in one order of magnitude.

For the same voltage signal in amplitude and frequency and the same fluid properties, the asymmetric co-planar array showed the lowest time-averaged flow of the three arrays. Flow in one order of magnitude higher than the asymmetric coplanar array was obtained with the traveling wave array, and the 3D array achieved a considerably higher flow than the traveling wave array and the asymmetric co-planar array (almost two orders of magnitude).

These results showed that the lowest fluid velocity is achieved by the asymmetric co-planar electrode array; the traveling wave electrode array achieves one order of magnitude higher than the asymmetric co-planar array, and the 3D electrode array is the configuration with the highest fluid flow. Both, the asymmetric co-planar array and the 3D array of electrodes generate a small back-flow that reduces the overall performance

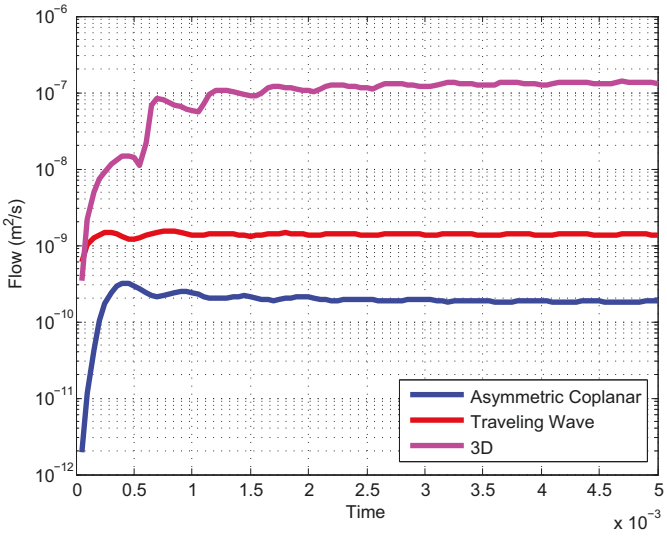

Figure 3.3: Comparison of the flow of the three geometries

of the micropump, while the traveling wave array of electrodes preserve a positive flow along all the applied signal cycles. However, the 3D electrode array implies a more complex and expensive fabrication process, compared to the other two electrode geometries. Furthermore, the travelling wave array requires the electrode biasing of three signals, offset by 90^{circ} for adjacent electrodes, which is translated into the use of expensive AC wave generators. For the case of this work, the asymmetric electrode array was chosen due to its low fabrication complexity and reduced costs, and for its straightforward biasing using typical wave generators.

3.2 Flow development for asymmetric coplanar electrodes

The model considers one pair of opposite electrodes with the electrodes' widths of $E_{\mathrm{N}} = 20$ µm and $E_{\mathrm{W}} = 60$ µm, a gap between the electrodes $g = 100$ µm, and a microchannel height $h = 100$ µm. A mesh with a total of 16760 elements was created using an element size of 25 nm at the electrode surface and increasing with the distance from this boundary. A total of 8 boundary conditions were defined in the 2D geometry, which are depicted in Figure 3.4, as well as their dimensions.

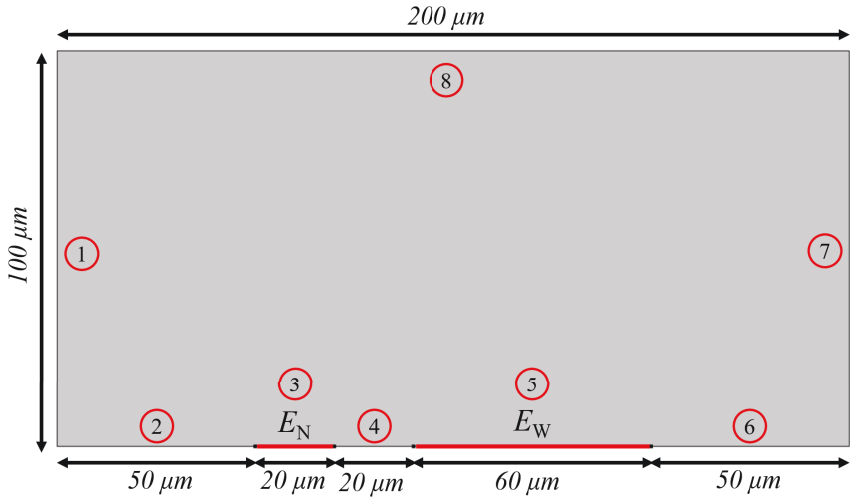

Figure 3.4: Geometry boundaries of the developed model. EN and EW correspond to the narrow and wide electrodes, respectively.

Table 3.5 shows the boundary conditions defined for each boundary, as well as for the complete domain, which comprises all the boundaries and the enclosed area.

Boundary	Electrostatics	Transport of Diluted Species	Laminar Flow
Domain	$\mathbf{E}=-\nabla V$ $\nabla\cdot(\varepsilon_0\varepsilon_r\mathbf{E})=\rho_v$	$\frac{\partial c_i}{\partial t}+\nabla\cdot\left(-D_i\nabla c_i-z_iU_{m,i}Fc_i\nabla V+\mathbf{u}c_i\right)=R_i$	$\rho\frac{\partial\mathbf{u}}{\partial t}+\rho(\mathbf{u}\cdot\nabla)\mathbf{u}=\nabla\cdot\left[-p\mathbf{I}+\mu\left(\nabla\mathbf{u}+(\nabla\mathbf{u})^T\right)\right]+\mathbf{F}$ $\rho\nabla\cdot(\mathbf{u})=0$
1	$V_{src}=V_{dst}$	$c_{i,src}=c_{i,dst}$ $-\mathbf{n}_{src}\cdot\mathbf{J}_{i,src}=\mathbf{n}_{dst}\cdot\mathbf{J}_{i,dst}$	$\mathbf{u}_{src}=\mathbf{u}_{dst}$ $p_{src}=p_{dst}$
2	$\mathbf{n}\cdot\mathbf{D}=0$	$-\mathbf{n}\cdot\mathbf{J}_i=0$	$\mathbf{u}=0$
3	$\sin(t)$	$-\mathbf{n}\cdot\mathbf{J}_i=0$	$\mathbf{u}=0$
4	$\mathbf{n}\cdot\mathbf{D}=0$	$-\mathbf{n}\cdot\mathbf{J}_i=0$	$\mathbf{u}=0$
5	$-\sin(t)$	$-\mathbf{n}\cdot\mathbf{J}_i=0$	$\mathbf{u}=0$
6	$\mathbf{n}\cdot\mathbf{D}=0$	$-\mathbf{n}\cdot\mathbf{J}_i=0$	$\mathbf{u}=0$
7	$V_{src}=V_{dst}$	$c_{i,src}=c_{i,dst}$ $-\mathbf{n}_{src}\cdot\mathbf{J}_{i,src}=\mathbf{n}_{dst}\cdot\mathbf{J}_{i,dst}$	$\mathbf{u}_{src}=\mathbf{u}_{dst}$ $p_{src}=p_{dst}$
8	$\mathbf{n}\cdot\mathbf{D}=0$	$-\mathbf{n}\cdot\mathbf{J}_i=0$	$\mathbf{u}=0$

Figure 3.5: Boundary conditions defined in the model for Electrostatics, Transport of Diluted Species and Laminar Flow modules.

The fluid velocity development was analyzed for four different frequencies (1 kHz, 10 kHz, 100 kHz, and 1 MHz) at 2 V_{PP} to observe the transient velocity evolution and its frequency dependence for a wide frequency range. The net flow evolution, from rest to the first 4 signal cycles, can be observed in the normalized plot on figure 7(a). The model suggests that for a fixed asymmetry ratio (60 μm : 20 μm), 1 kHz signal achieves one order of magnitude higher velocities that the 10 kHz signal, while for higher frequencies (100 kHz and 1

MHz), the net flow becomes negligible. A fast flow development can also be noticed, where the flow is fully developed after four cycles for every case. The pulsating nature of the flow (as easily seen from the inset in figure 7(a)) follows the magnitude of the induced electric field as the AC amplitude evolves through time. Furthermore, the net fluid velocity development for frequencies from 1 to 10 kHz, as plotted in figure 7(b), confirms an exponential velocity decay, even at small frequency steps.

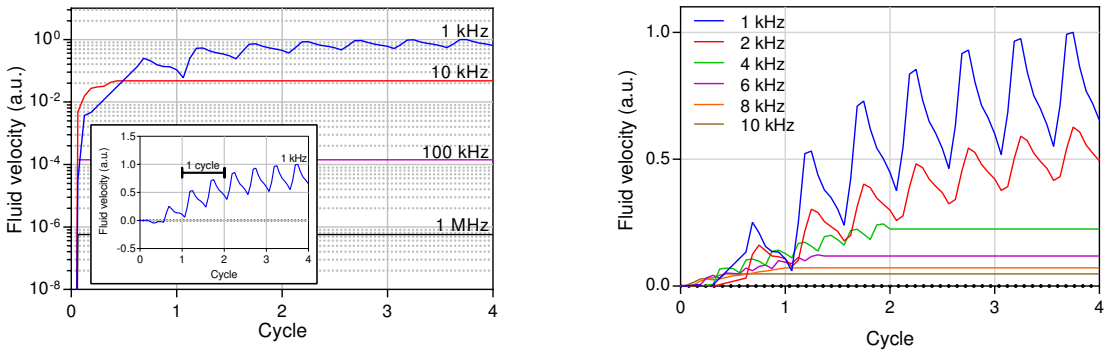

(a) 1 kHz to 1 MHz

(b) 1 kHz to 10 kHz

Figure 3.6: Fluid velocity simulation results: (a) normalized fluid velocity for four AC frequencies at 1 V_{PP}: 1 kHz, 10 kHz, 100 kHz and 1 MHz. Inset shows net fluid velocity evolution of the 1 kHz AC signal in a linear y-axis scale. And (b) normalized fluid velocity for frequencies from 1 kHz to 10 kHz. Fluid velocities are shown as arbitrary units (a. u.).

The sequence of images in figure 8 shows the evolution of the vortices (numbered from 1 to 4 from left to right) once the net flow is fully developed in the forward direction (fourth cycle from figure 7 for 1 kHz) throughout half a cycle of the applied signal. Even though the vortices direction is sustained in an alternating electrode polarization, figure 8(a) and (b) show a slight velocity decrease as the AC magnitude increases (this effect is also visible as a small notch in the fluid velocity plot for 1 kHz in figure 7). This is likely caused by charge reordering at electrodes surface as the polarizing signal switches, since co-ions are dispelled, and counter-ions are attracted to form an EDL to satisfy electrostatic equilibrium. As the maximum AC amplitude is reached, vortex 3 becomes dominant over vortices 1, 2 and 4, thus strongly establishing a net flow at this point (figure 8(c)). Finally, all four vortices lose strength as the AC magnitude decreases to complete a cycle (figure 8(d) and (e)).

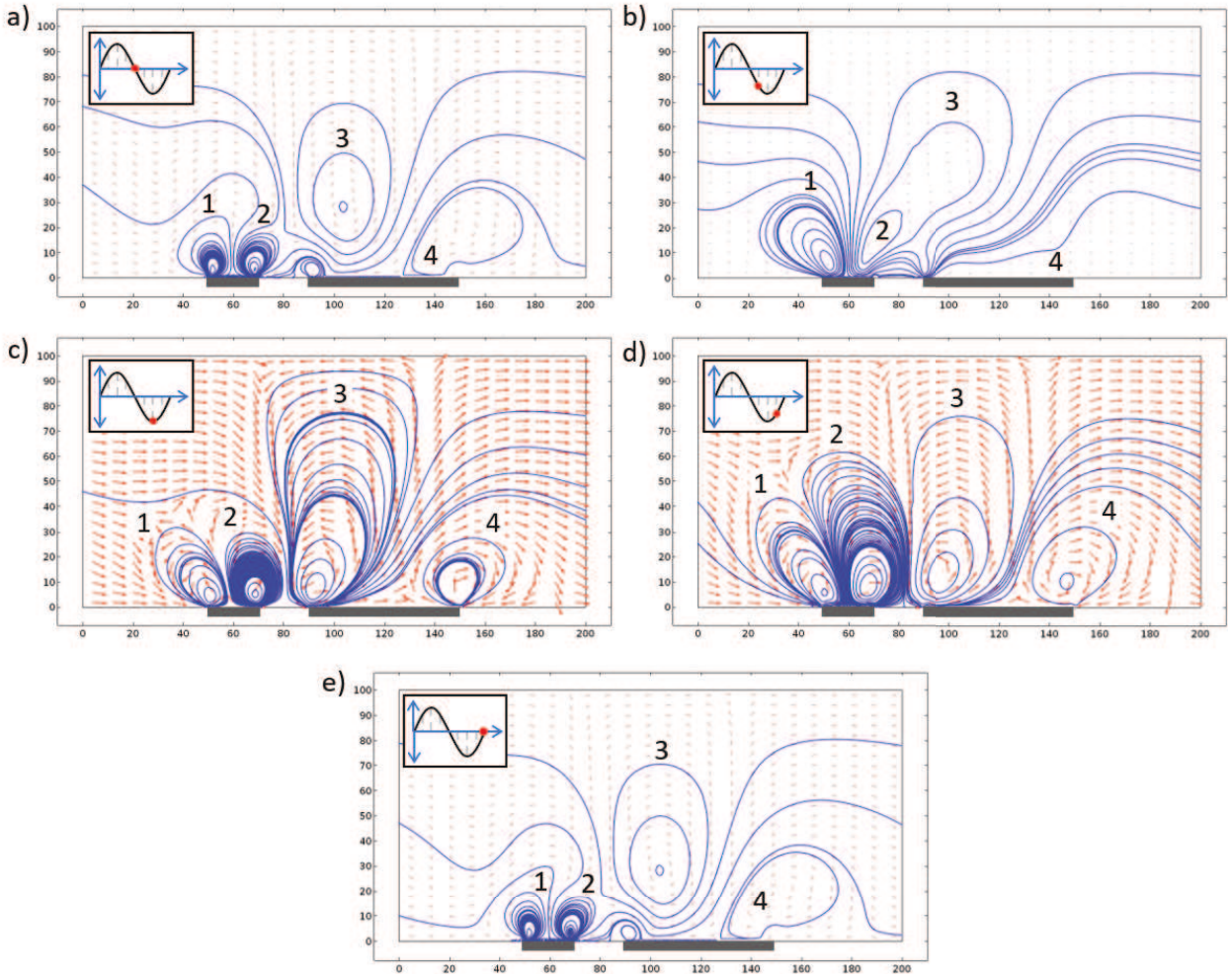

Figure 3.7: Finite element analysis of vortex formation along the second half of the fourth cycle of the applied AC signal at 1 kHz (fully developed flow): (a) 3.5 ms, (b) 3.625 ms, (c) 3.75 ms, (d) 3.875 ms, and (e) 4 ms. Insets show the AC cycle step. Arrows' lengths indicate the velocity magnitude and direction, whereas the streamlines depict the vortex shape.

Chapter 4

Fabrication and characterization of glassy carbon microelectrode arrays

In the semiconductor industry, different types of photoresist are used as a protective/sacrificial material to etch silicon and metals by means of wet or dry processes to develop transistors and other microelectronics components. In C-MEMS, photoresist is used as the carbon precursor not only for static but also for dynamic structures [67], such as microelectrodes, suspended beams, accelerometers, among others.

The conventional Carbon-MEMS (C-MEMS) fabrication process comprises two elemental steps: photolithographic patterning of a carbon precursor, followed by its thermal decomposition—or pyrolysis—to obtain a carbonaceous material. In photolithography, patterns from a stencil are transfered to a photosensitive material deposited on a substrate. Then, the subsequent thermal decomposition of the patterned structures at temperatures between 600-1100°C in an oxygen-free environment allows the release of non-carbon element to the environment, thus yielding the characteristic glassy carbon material. Two distinctive features of this process are straightforwardness and low-costs for feature sizes down to ∼10 microns, since no costly and difficult-to-operate equipment is required, nor specialized facilities such as high-class cleanrooms.

A wide variety of carbon precursors are available for this purpose, though the most typical are the polymeric resins [68, 69]. The resulting material properties, mainly including volumetric shrinkage amount, pore size and density, and electrical conductivity, are dependent on the pyrolysis conditions, that include temperature ramp rate, maximum pyrolysis temperature and inert-gas flow rate [68]. By means of this process setup, satisfactory chemical, electrical and mechanical properties have been demonstrated for a wide range of applications in electrochemistry, electrokinetics, mechanical sensing, among others.

In this work, the convenitonal photolithography process was followed to fabricate high-aspect-ratio (HAR) microstructures on top of asymmetric coplanar interdigitated electrode arrays (IDEAs), and pyrolized all together under conditions that have been previously studied in detail for electrokinetic applications [56]. For this purpose, two patterning steps were followed: (*i*) patterning of IDEAs on a substrate and (*ii*) patterning of HAR structures on top of the IDEAs. Pyrolysis was only carried out after the two-step patterning to guarantee effective electrical contact between the two patterned layers. The complete fabrication procedure followed for this purpose is detailed in this chapter, as well as the devices preparation for experiental testing.

4.1 Design of microelectrode arrays for ACEO pumping

The first step on fabrication of microstructures by photolithography is the 2D layout of the structures to be fabricated—often referred to as geometries or polygons—using a computer-aided design software. There is already specialized software for this purpose on the market such as Coventorware, IntelliSuite, ProCAETool, MEMScap, SOLIDIS, among others for MEMS designs, but also general purpose tools such as AutoCAD and DraftSight can be used in the case of relatively low-complexity structures, as in this work. The purpose of using this specialized software is to optimize the development process by means of reducing the cost and time expended on the mask design stage, but one of the main drawbacks is that these tools usually are costly and the learning process can be slow. For highly-customized designs and with a low number of layers (≤ 3), the photomask design process is simpler using a general purpose software—AutoCAD in this case.

The resulting photomask is an stencil with layed out polygons that block the UV light and openings that are transparent to the light. For this reason, the photomask are designed according to the type of photoresist (PR) to be used to pattern the structures. The type of photoresist is determined by the effect of the UV rediation producess when the PR is exposed to it. For positive photoresist, the exposed regions become soluble to the developer thus are subsequently removed from the substrate; whereas for negative PR, the exposed areas are crosslinked—or polymerized—, making it difficult to dissolve and remove them.

Figure 4.1 depicts the type of photomask used for each type of PR to obtain an hypothetical interdigitated electrode array. The desired structure to fabricate is shown in Figure 4.1(a). Then, Figure 4.1(b) shows the type of mask used for negative PR, where white areas represent the UV-transparent areas, meaning that the actual IDEA geometry undergoes UV esposure. In contrast, the mask shown in 4.1(c) is the negative projection of the IDEA structure, thus the exposed areas are all the PR but the actual IDE geometry.

Both types of PR have been used to fabricate C-MEMS structures, showing acceptable results in terms of electrical conductivity, porosity and elasticity, but besides thin films, negative PR is often preferred due

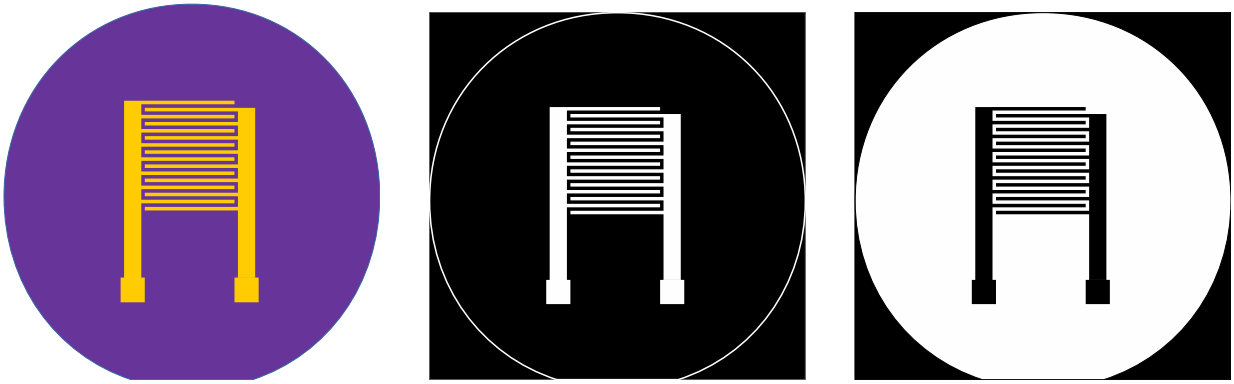

(a) Photoresist electrodes (b) Negative photomask (c) Positive photomask

Figure 4.1: Representation of the photomasks used for photolithographycally patterning of interdigitated electrode arrays for (a) Photoresist electrodes (yellow) developed on the substrate (purple); (b) negative photoresist and (b) positive photoresist photomasks. White represents UV transparent film and black inked areas.

to the variety of viscosities available, which allows to obtain a wide range of structure thicknesses, ranging from 0.5 µm up to ∼200 µm, for the case of the SU-8 photoresists made by MicroChem Corporation.

In this work, SU-8 negative photoresist was used to pattern the structures. The viscosity of the SU-8 was selected depending on the desired height of the structures, and the post-pyrolysis shrinkage amount was considered for this purpose. As UV radiation is used to transfer the patterns from the photomask to the photoresist on the substrate, the base material of the photomask has to be chosen depending on the wavelenght of the UV radiation to be applied to the photoresist. In turn, the type of PR to be used defines the wavelenght of the UV light. Fortunately, low-cost transparency films are suitable for this purpose and are widely used [70] for feature sizes down to 10 microns[1]. The photomasks were printed out on a Fuji 0.007"-thick transparency film on a resolution of 25,400 DPI for a minimum feature size of 0.0004"/10 µm (CAD/Art Services, Inc. Bandon, OR, USA). As SU-8 negative PR is used as carbon precursor, the geometries to be crosslinked should be transparent in the stencil, as depicted in 4.1(b). Two different masks were designed for the carbon structures:(i) the planar interdigitated electrode arrays, and (ii) squares and rectangules to create the HAR structures with a thick SU-8 layer, which are lined up to the IDEAs.

4.2 Photolithographic patterting of SU-8

As mentioned before, a two-step process was employed in this work to develop: (*i*) planar electrodes, followed by (*ii*) high-aspect-ratio microposts. All the electrode arrays were fabricated following the conventional

[1]Early years of last decade, Intelligent Micro Patterning System Solutions, LLC, introduced a gray-scale fabrication system to reduce manufacturing cost and time for microfluidics and BioMEMS by means of laser patterning directly onto the surface of the photosensitive material, thus avoiding the need of a physical mask.

Carbon-MEMS process, which comprises photolithographic patterning of an organic carbon precursor, followed by pyrolysis. The fabrication process was carried out inside a class 1000 cleanroom at 22°C and 38.4% relative humidity. All the structures were fabricated using 4-inch, P-type (boron-doped) silicon wafers ⟨100⟩ with a 5000 Å ± 5% oxide (SiO_2) layer, as the bulk material. These wafers have a sheet resistance of 40-100 Ω-cm and a thickness of $500 - 550$ µm (NOEL Technologies, Campbell, CA, USA)[2]. The wafers were cleaned using acetone, isopropyl alcohol and deionized water; then dried with N_2. After clean up, the wafers were dehydrated in an 120°C oven for $20 - 30$ minutes. Figure 4.2 depicts the process followed to fabricate both, the planar electrode and the HAR microposts.

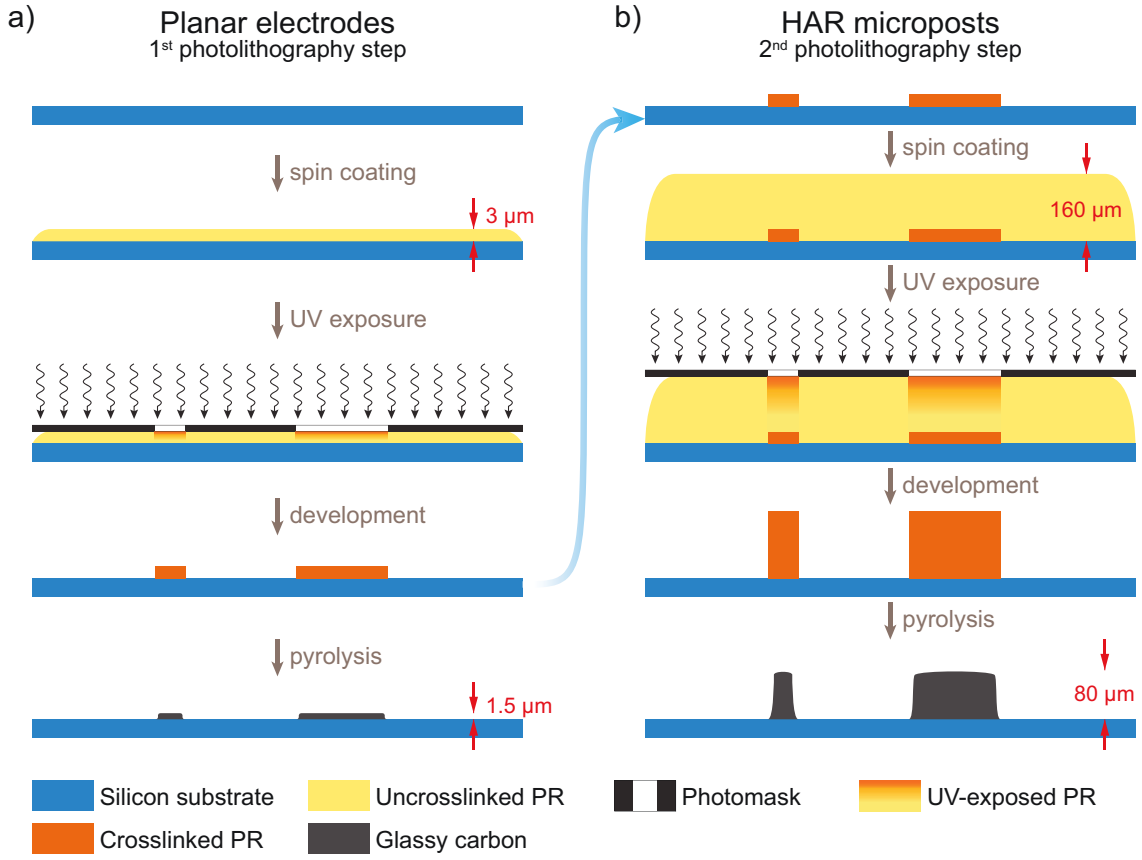

Figure 4.2: Two-step photolithography process to fabricate planar and high-aspect-ratio microstructures

4.2.1 Asymmetric coplanar electrodes

Before any PR coating, the substrates surface was cleaned to maximize adherence between PR and SiO_2 layer. Solvent remains or moisture increase the risk of photoresist to peel off the substrate during development or

[2]Silicon nitride (Si_3NO_4) wafers have been demonstrated to achieve a better performance for electrochemistry applications when using glassy carbon electrodes; however, silicon dioxide (SiO_2)-pasivated wafers were prefered due to their lower cost and comparable performance [56].

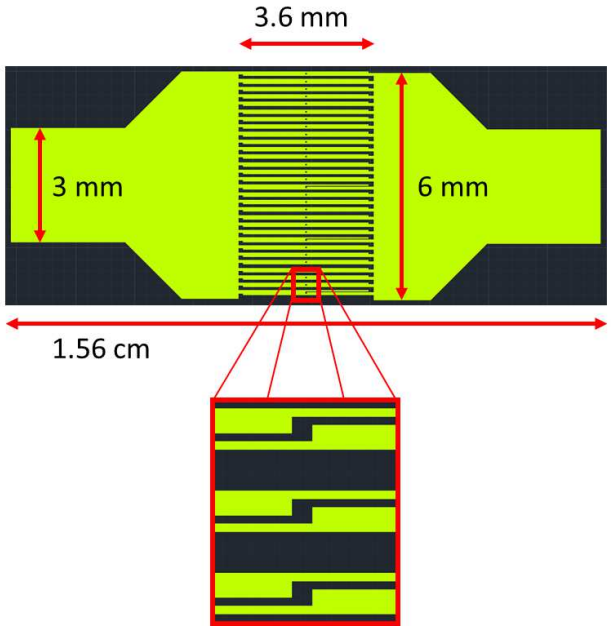

Figure 4.3: Electrode geometry and width switch.

pyrolysis. For this purpose, wafers were rinsed with acetone, isopropyl alcohol and deionized water, and then dehydrated for 30 minutes in a convection oven at 120°C.

Three different designs of planar electrodes were evaluated in this work, where the difference among them relies on the asymmetry ratio between the wide and the narrow electrode widths, E_{W} and E_{N}, respectively. Taking a base width of 20 µm for E_{N}—which was also taken as the base gap distance between electrodes—E_{W} was set to 60 µm, 80 µm and 100 µm for each design. The inner gap, G_{I}, and outer gap, G_{O}, were set to 20 µm and 100 µm, respectively. At the middle of each electrode comb finger, they switch width from E_{W} to E_{N} and viceversa, while keeping G_{I} and G_{O} constant, thus on the second half of the fingers the arrangement of the electrodes is geometrically inverted, as depicted in Figure 4.3.

The reason of the electrode width switching is that the microfluidic channel was designed to be cyclic, thus on the first half of the channel the fluid is pumped in one direction and on the second half, it is on the opposite direction. With this cyclic flow, the hydrostatic pressure gradients on each side of the channel is minimized, thus allowing the fluid to move only by the electrokinetic effect.

The planar electrodes were fabricated following the standard photolithography process to a photoresist thickness—before pyrolysis—of 3 µm. For this purpose, SU-8 2002 photoresist was used, since it allows a spin-coating thickness range between 2 to 3 µm. In this case, SU-8 2002 photoresist (PR) (MicroChem, Westborough, MA, USA) was spin-coated on the substrate at 1000 rpm for 30 s to a thickness of 3 µm using a commercial spin-coater (WS650SZ-6NPP, Laurell Technologies, North Wales, PA, USA). Wafers

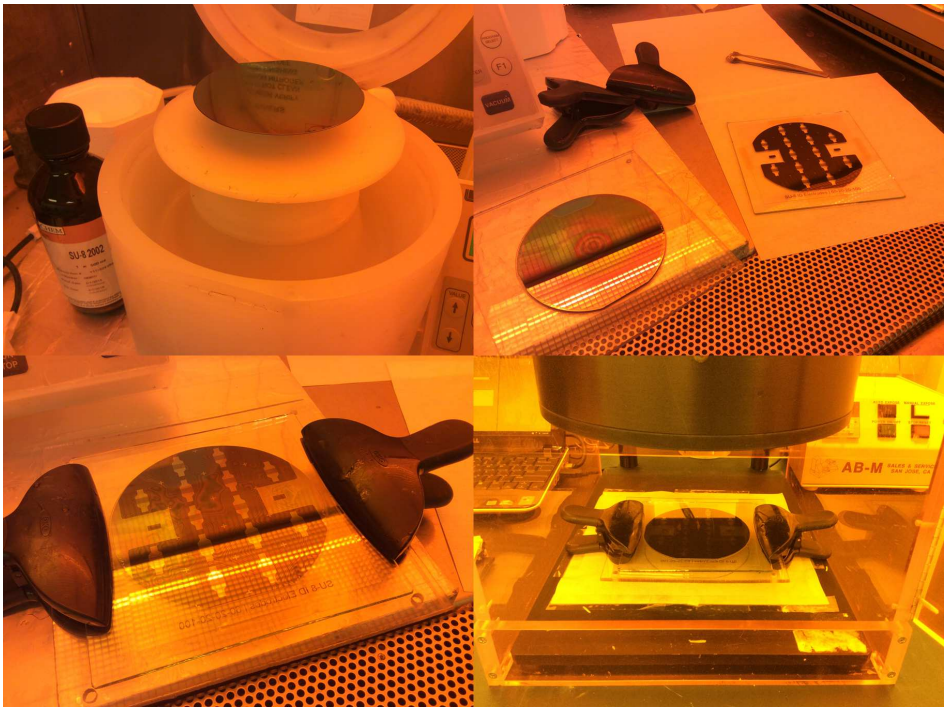

Figure 4.4: First photolithography process—planar electrodes.

were centered on the spinner chunk to allow uniform distribution of the photoresist and, to avoid bubble formation, the resin was poured onto the surface directly from the original container. Usually, bubbles are easy to remove when using low-viscosity resins, but for those highly viscous, this could take several minutes and vacuuming was not considered due to the risk of uncontrolled UV exposition. The proper amount of photoresist poured on the substrate surfaces is also important in this process because if this amount is much greater than the recommended by the manufacturer and the photoresist is highly viscous, there is a risk of photoresist buildups at the edges of the wafer, which will affect the final height of the structures on this area of the substrate. Figure 4.4a shows the silicon wafer after the first spin coating step.

Right after spin coating, the wafers were placed on a hot plate at 95°C for 2 min for soft-baking. With this step, temperature helps the deposited photoresist to evaporate solvents, and to evenly distribute the layer all over the substrate surface in case of build-ups; however, as experienced during previous attempts, this only works for small accumulations of material.

After letting the wafers to cool down once soft-baked, and the photoresist had hardened up, the planar-electrodes photomask was faced off against the resin with the inked side of the mask in direct contact with the resin, as shown in Figures 4.4b and c. This cannot be done before the photoresist has hardened enough, since the mask could get smeared on resin. Plastic clamps were used to firmly attach the wafer to the photomask and then placed on the flood exposure system to expose to a dose of 90 mJ/cm^2 (Figure 4.4d), using a near

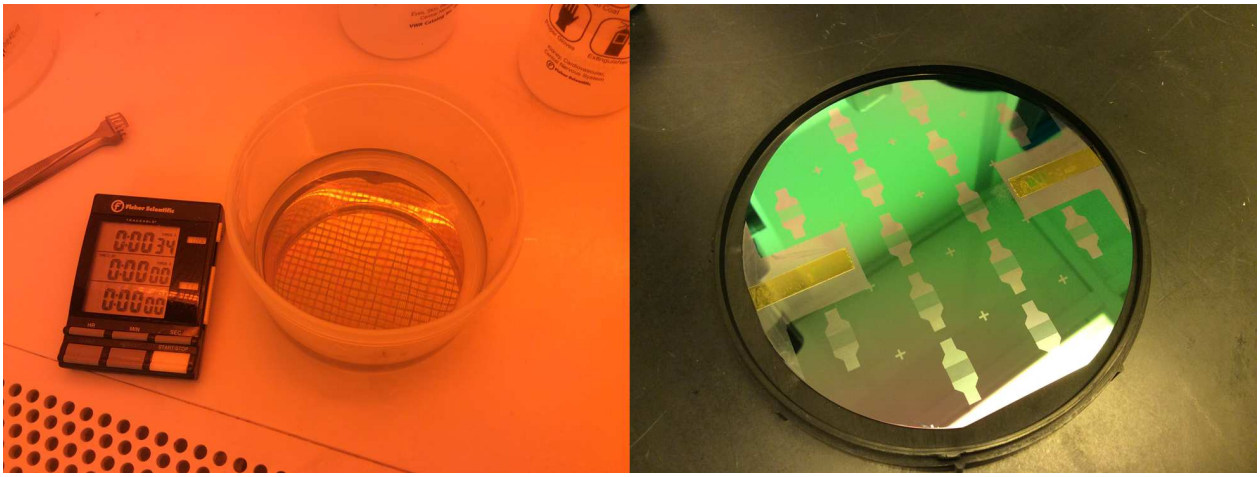

Figure 4.5: Final structures

UV light (350-450 nm) flood exposure system (AB&M Inc., Scotts Valley, CA, USA) to trigger crosslinking of the exposed resist. Also, if the inked side of the mask is not in direct contact with the resin, light diffraction will affect the accuracy of the feature sizes of the mask. The correct exposure time has to be calculated to apply the right dose of radiation to the resin, depending upon its thickness and viscosity. Underexposure will lead to undesired removal of material during development, and overexposure will cause larger features than desired.

A post-exposure bake (PEB) was carried out to complete the crosslinking reaction started during the exposure and improve adhesion of the crosslinked structures to the substrate. This was carried out at $95°C$ for 2 min. During this process, the transfered patterns start to be visible due to the difference in densities between crosslinked and uncrosslinked photoresists—if this is not the case, the photoresist was likely underexposed.

The last step was development, where the uncrosslinked photoresist is removed from the substrate using developer solution. For the case of the planar structures, the structures were just rested in the developer solution for 1 min, allowing diffusive transport to act on the photoresis. Agitation—convective transport—was an important parameter for a proper development for high aspect ratio structures. Figure 4.5a and b shows the development step for these devices and the resulting wafer with the patterned microstructures, respectively.

4.2.2 High-aspect-ratio microposts

Fabrication of high-aspect-ratio microposts on top of the planar electrodes is more challenging. To be able to align both layers, a mask aligner was required before UV exposure of the second layer. In this case, to

Table 4.1: Photolithography parameters for high-aspect-ratio microposts using SU-8 2050.

Process step	**Value**
Spin coating velocity	500 RPM for 10 sec with 100 RPM/sec, then 1000 RPM for 30 sec with 300 RPM/sec
Soft baking	2 min at 95°C
UV exposure energy	90 mJ/cm^2
Post-exposure baking	2 min at 95°C
Development time	1 min

pattern HAR microposts, a second layer of resist (SU-8 2050 (MicroChem, Westborough, MA, USA)) was spin-coated directly over the recently-developed planar structures at 1000 rpm for 30 s, to a thickness of 160 µm. The second PR layer was soft-baked at 65°C for 7 min, and then at 95°C for 35 min. For the second UV exposure step, the microposts photomask was aligned to the underlying PR electrode structures using a mask aligner (MA56, Süss MicroTec, Garching, DE), and then UV exposed under energy flux of 270 mJ/cm^2. Post-exposure baking was carried out at 65°C for 5 min, and at 95°C for 13 min. Finally, the HAR structures were developed for 16 min with SU-8 developer (MicroChem, Westborough, MA, USA) on an orbital shaker (3520, Labline Instruments, Maharashtra, IN) at 70 rpm to allow the developer to permeate small gaps between adjacent microposts.

4.3 Pyrolysis

Once the planar and high-aspect ratio structures were developed, the final step: chemical decomposition—or carbonization/pyrolysis—step was carried out to obtain the final glassy carbon material. All the structures were pyrolyzed in an open-ended quartz tube furnace (RD-M, R.D. Webb Company, Inc., Natick, MA, USA). Once the samples were placed in the tube, a high purity N_2 gas flow was diffused across the tube for 10 min at room temperature at a rate of 2.4 l/min to remove any oxygen trace—the N_2 flow was kept constant throughout the entire process. The tube temperature was then increased from room temperature to 300°C at a rate of 5°C/min and maintained at 300°C for 1 hour and then ramped up from 300°C to 900°C at a rate of 10°C/min and maintained at that maximum temperature for 1 hour. The furnace was then turned off to allow the samples to passively cool down to room temperature. The N_2 flow was stopped when the tube cooled down to 150°C.

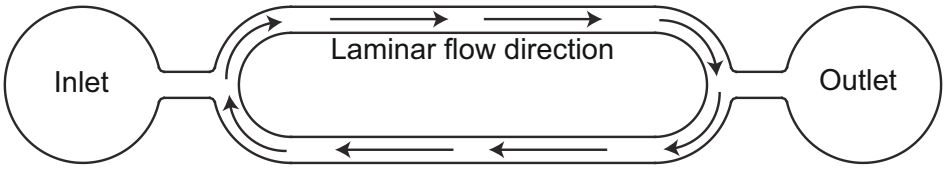

Figure 4.6: Loop microchannel design and laminar flow to avoid hydrostatic pressure effects on the fluid velocity.

4.4 Microfluidic device assembly and experimental setup

PDMS microfluidic channels were prepared using soft-lithography—a low-cost process widely used to fabricate microfluidic devices [71]—to serve as testing chambers of the IDEs. Instead of the commonly-used linear channels, a loop channel was designed in this work to prevent hydrostatic pressure differentials to perturb the electroosmotic pumping caused by the electrodes. Ideally, the laminar nature of the fluid flow prevents fluid from the inlet and outlet to enter the loop channel. The microfluidic channel is depicted in Figure 4.6.

To fabricate the PDMS microchannels, an SU-8 layer with a thinkess of 100 μm—the desired microchannel height—was patterned on a silicon wafer with the negative impression of the microchannel; this is, the actual microchannel shape was crosslinked. Then, PDMS was poured over the master to pattern the positive impression of the microchannels on the PDMS. The hardened PDMS chunk and the IDEs were exposed to oxygen plasma treatment for two minutes at 30 W and 150 mTorr, to activate the surfaces of both, PDMS chuck and glass substrate for irreversible bonding[3]. The PDMS chunks were manually lined up to the IDEs under an optical microscope and bonded with the carbon pads exposed.

The carbon pads were designed to facilitate electrical connections to the signal generator. The pads were first covered with a thin tin layer and then soldered to copper wires. Since tin and carbon juntions are not strong enough—has opposite to carbon/indium juntions—attachment of the wires to the pads had to be strengthen and protected by covering the soldered joint with a fast epoxy resin. To accelerate the hardening of the resin, the devices were heated to 80°C on a hot plate. The final device, ready for experimental testing, is shown in Figure 4.7.

The experiments were carried out under an optical microscope with a CCD camera attached for video recording. Ten-second videos were recored once the flow was fully developed and processed later using ImageJ sorfware with a particle tracking plugin (U.S. National Institutes of Health, Bethesda, MD, USA). The devices were electrically stimulated using a waveform generator (33210A, Agilent Technologies, Santa Clara, CA, USA) and the applied signal was monitored by an oscilloscope (TDS 2014B, Tektronix Inc., Beaverton, OR, USA). The fluid velocity was determined in a frequency range from 1 kHz to 1 MHz and for

[3]Surface activation occurs by the creation of Si−OH groups, where the reactive $-OH$ groups form a covalent Si−O−Si bond when the surfaces are put in contact [72]

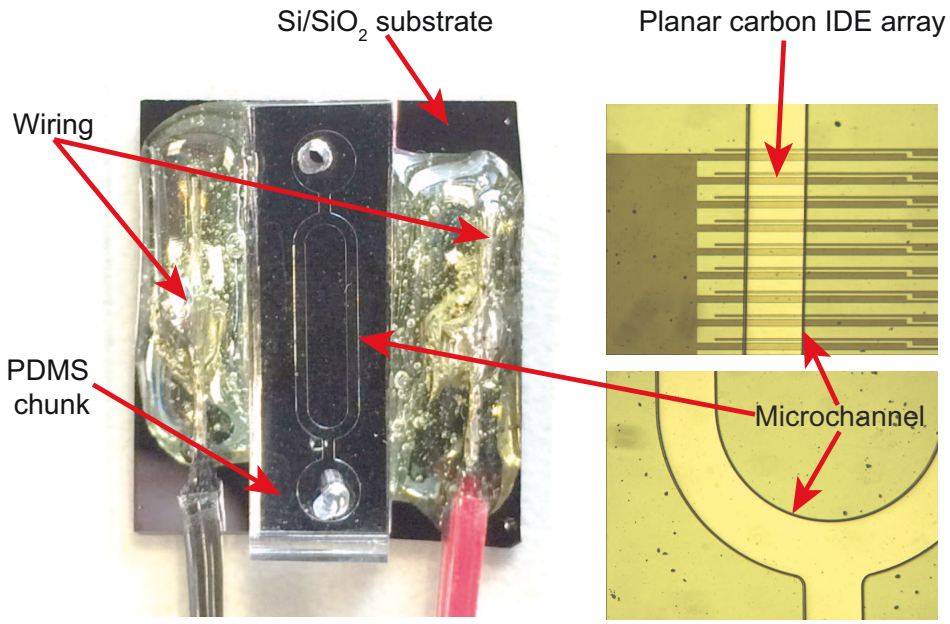

Figure 4.7: Microfluidic device prepared for experimental testing.

amplitudes ranging from 2 to 20 V_{PP}. Figure 4.8 shows the setup used for the experiments.

The fluid propulsion mechanism comprises two pumping chambers containing electrode pairs confined in the PDMS microchannel (see figure 4.9). Three asymmetry ratios for the wide and narrow electrodes, E_W/E_N, were utilized for the planar electrodes: (*i*) 60 µm : 20 µm, (*ii*) 80 µm : 20 µm, and (*iii*) 100 µm : 20 µm. Furthermore, devices (*iv*), (*v*) and (*vi*) were fabricated by developing 80 µm-height (after pyrolysis) HAR microposts on top of a separate set of planar electrodes with the same asymmetry ratios as those of (*i*), (*ii*) and (*iii*), respectively. In all cases, the inner gap (i.e., the distance between opposite electrodes of the same pair) is $G_I = 20$ µm, and the outer gap (i.e., distance between consecutive electrode pairs) is $G_O = 100$ µm. The total length of each pumping chamber is 6 mm, thus containing 30, 27 and 25 electrode pairs for devices (*i*) and (*iv*), (*ii*) and (*v*), and (*iii*) and (*vi*), respectively. Electrode fingers are 3.6 mm long, and each electrode pair switches widths ($E_W \leftrightarrow E_N$) halfway from base to the outer end of the finger, while preserving inner and outer gap lengths, as shown in the inset of figure 4.9. The flow direction is split into forward and reverse regimes, determined by the direction of the net flow with respect to the electrode arrangement: forward for a flow going from E_N, through G_O, toward E_W; and reverse for a flow in the opposite direction [35, 36], as depicted in the inset of figure 4.9.

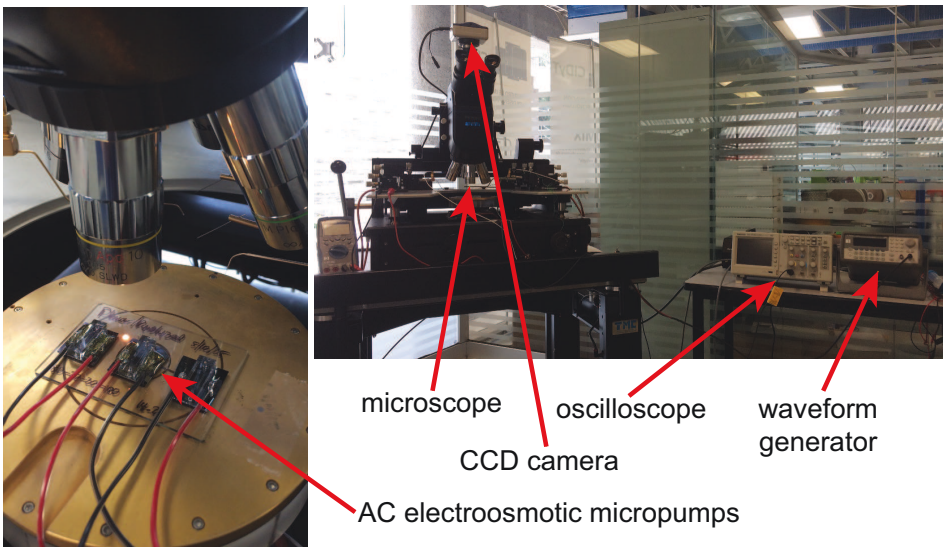

Figure 4.8: Experimental setup of the AC electroosmotic micropumps.

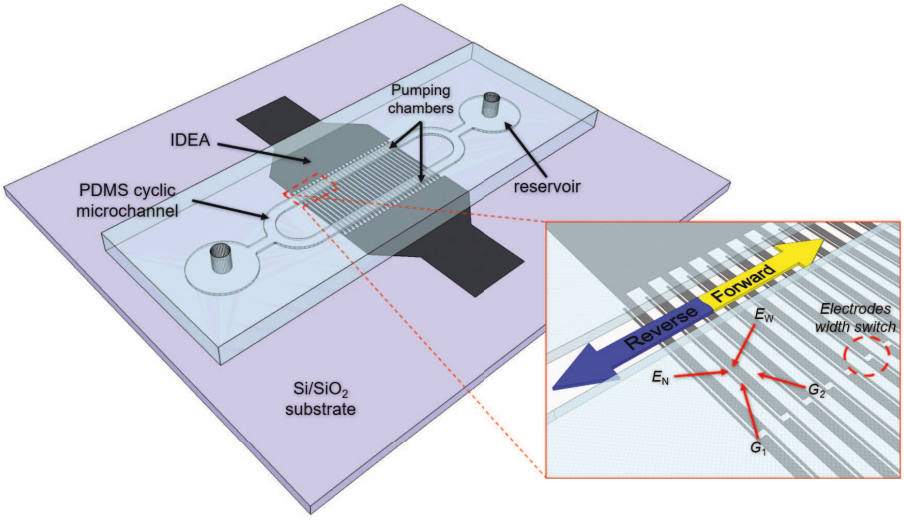

Figure 4.9: Schematic diagram of the assembled microfluidic chip. The glassy carbon interdigitated electrode array (IDEA) is patterned on the silicon substrate, and the fluid is driven inside the cyclic microchannel by two pumping chambers. The inset shows one pumping chamber and forward flow from E_{N} through G_{O} towards E_{W}, and the reverse flow going in the opposite direction; the electrode width switch is also shown halfway from electrode base to tip for both combs.

4.5 Glassy carbon structural characterization

Thickness and volumetric shrinkage of the resulting carbon structures were characterized using confocal microscopy (Axio CSM 700, Carl Zeiss AG, Oberkochen, DE). Physical inspection and imaging of microstructures were carried out by scanning electron microscopy (SEM) (EVO MA25, Carl Zeiss AG, Oberkochen, DE). Elemental composition of the pyrolyzed material was determined by Energy Dispersive Spectroscopy (EDS) (XFlash 6—10, Bruker Corp., Billerica, MA, USA). The electrochemical properties of the pyrolyzed carbon depend upon the type of carbon precursor and the pyrolysis conditions. Raman spectroscopy (inVia Raman microscope, Renishaw, UK with 514 nm Argon laser, Modu-Laser, LLC, Centerville, UT, USA) was used to determine the graphitic (sp^2) and amorphous carbon (sp^3) crystallites content of the electrodes.

A testing solution of distilled water (with a conductivity of $\sigma_f = 5.5$ µS/cm) containing 1 µm-diameter latex tracers was prepared for experiments. The tracer's size was determined not only considering a favorable visibility under a microscope with a 10× objective, but also to avoid dielectrophoretic effect that might disturb the particle's velocity on the proximity to the electrodes' surface. All microfluidic devices were degassed for 15 min, and the testing solution was immediately pipetted into the fluidic chambers to avoid bubbles in the microchannels. The electrodes were powered by a sinewave generator (33210A, Agilent Technologies, Santa Clara, CA, USA), while an oscilloscope (TDS 2014B, Tektronix Inc., Beaverton, OR, USA) was used for signal monitoring. Experiments were carried out at the following working frequencies, f_w: 1 kHz, 2 kHz, 10 kHz, 20 kHz, 100 kHz, 200 kHz and 1 MHz. For each frequency, the signal amplitude was swept from 2 to 20 V_{PP} in 2 V_{PP} steps. The operation of the devices was monitored by an optical microscope (PS-888, Seiwa Optical, Tokyo, JP) with an attached camera (Motic 3000, Motic Instruments, Xiamen, CN) to record 30 s long video clips for each test condition once the flow was fully developed. The fluid velocity was then measured by tracking 10 tracers throughout different video frames using a particle tracking software (ImageJ, National Institutes of Health, Bethesda, MD, USA), to later compute their average velocity.

During pyrolysis of the polymeric precursor, non-carbon elements in the material's molecular structure are sublimated, while the remaining carbon atoms are reconstituted, forming sp2 and sp3 carbon [37]. Carbonization leads to isometric shrinkage and considerable increase of electrical conductivity of the pyrolyzed material. Figure 4.10 shows SEM micrographs of the coplanar and HAR microelectrodes of different asymmetry ratios after pyrolysis.

Before pyrolysis, the height of the coplanar and HAR structures averaged 2.98 µm and 159.74 µm, respectively. Average heights after pyrolysis are 1.28 µm and 75.09 µm for coplanar and HAR structures, respectively, corresponding to a total vertical shrinkage of 57% and 53%. Besides pyrolysis conditions, overall

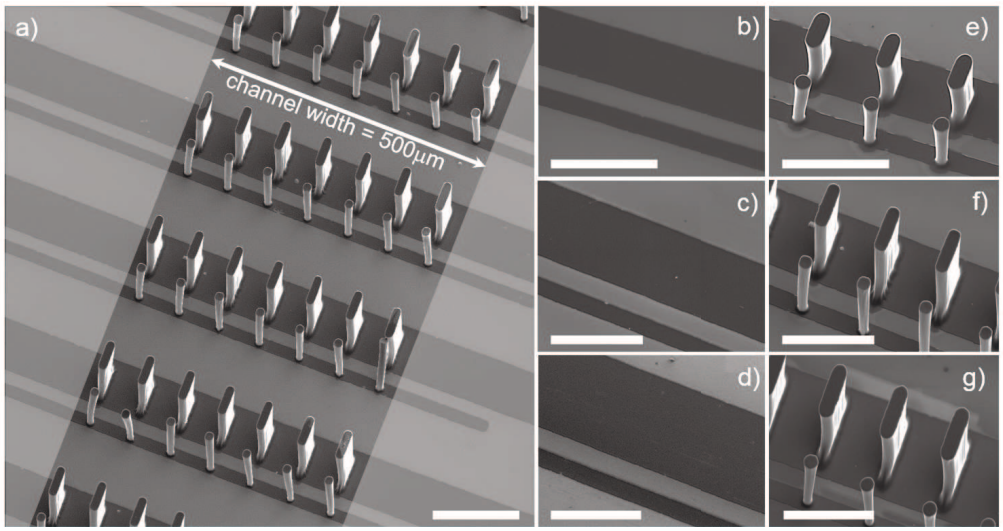

Figure 4.10: Scanning electron micrographs of the fabricated glassy carbon asymmetric coplanar electrodes and high-aspect-ratio (HAR) microposts. (a) Asymmetric coplanar electrodes with HAR microposts. Coplanar and coplanar with HAR microposts asymmetry ratios, respectively: (b,e) 60 μm : 20 μm, (c,f) 80 μm : 20 μm and (d,g) 100 μm : 20 μm. Scale bars = 100 μm.

shrinkage strongly relates to pre-pyrolysis geometry of the structures. For instance, for coplanar electrodes, a larger vertical shrinkage is attained for the narrower geometry: 58% for device (i), 56% for device (ii) and 53% for device (iii) (i.e. shrinkage percentage decreases as the electrode broadens) suggesting an increasing lateral stress caused by the combination of high temperature and strong adhesion of the pyrolyzed structure to the substrate. This effect is yet more evident for the case of HAR microposts, where the structures have a small base area compared to their vertical dimensions, thus lateral and vertical shrinkages contribute considerably to the volume reduction, averaging 77%, 83%, and 78% for devices (iv), (v) and (vi), respectively. Other parameters, such as temperature and gas pressure fluctuations inside gas furnace can also affect the shrinkage variations.

Elemental composition obtained from EDX analysis of the pyrolyzed structures are shown in figure 4.11(a) and (b) for both, coplanar and HAR structures, respectively. Planar electrode samples' composition analysis indicates presence of Carbon (55.13 atomic %), Silicon (18.45 atomic %) and Oxygen (26.42 atomic %). The last two elements are the components of the SiO2 film on the substrate underneath and around the electrodes and probing of the silicon dioxide was due to the penetration depth of the electron beam used for the measurements. No other elements were found in the pyrolyzed material.

EDX spectrum for the HAR structures, in turn, shows a prevailing presence of Carbon (96.02 atomic %), whereas oxygen content is considerably minor (3.98 atomic %) and Silicon is absent. These results are due to the fact that the electron beam was located on top of the micropost, thus reducing the electron beam

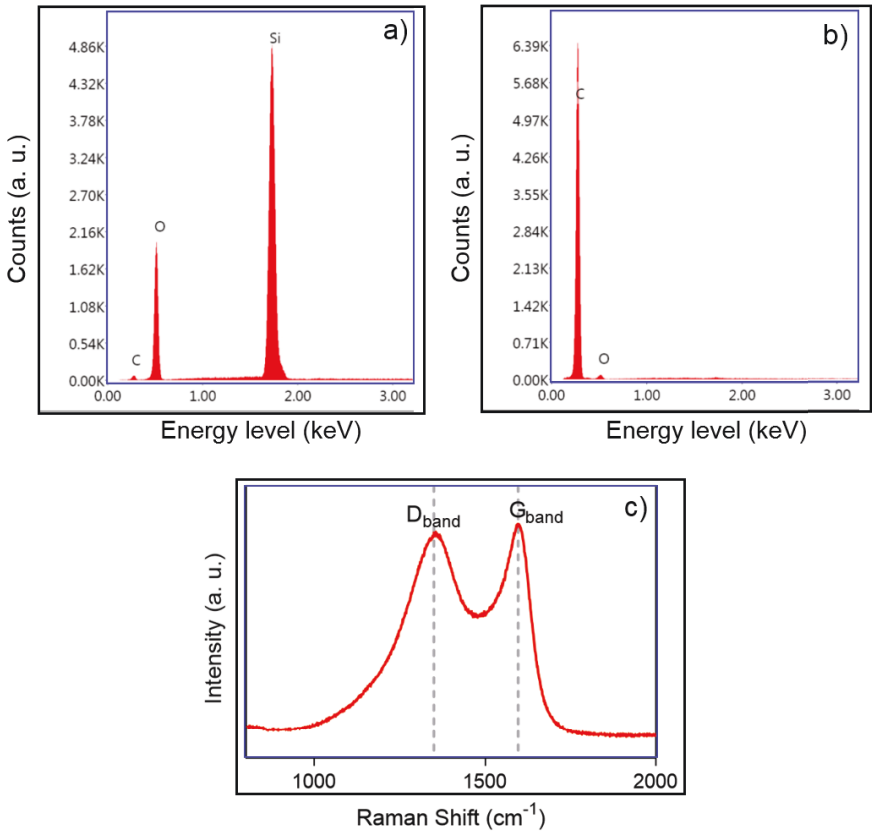

Figure 4.11: Energy-dispersive X-ray (EDX) and Raman spectrums of pyrolyzed carbon structures for: (a) planar electrodes; (b) high-aspect-ratio microposts. Si and O peaks shown on plot (a) resulted the SiO_2 film probed due to penetration depth of the EDX electron beam ($\sim$ 20 µm), and (c) Raman spectra of the carbon electrodes fabricated by pyrolyzing SU-8 2002 photoresist at 900°C for 1 h.

interaction with the substrate.

Figure 4.11(c) shows the Raman spectrum of the pyrolyzed carbon material. D- and G-bands, typically seen in glassy carbon, were found at 1355 cm^1 and 1597 cm^1, respectively. The D-band indicates the presence of sp^3 amorphous carbon structures, while the G-band is characteristic of sp^2 carbon networks forming graphitic nano-crystallites. The G-band for single crystal graphite is usually found at 1575 cm^1, and the band shift is caused by an extremely small crystallite size present in the structure [73]. The intensity ratio of the D-band to the G-band (I_D/I_G) defines the degree of structural disorder with respect to a perfect graphitic crystallite, and consequently, the crystallite size is inversely proportional to this ratio: $1/La \propto I_D/I_G$. The I_D/I_G ratio of the pyrolyzed carbon in this work measured 0.96, indicating that the carbon structure is formed by equivalent amounts of ordered (sp^2) and disordered (sp^3) carbon [74]. From EDX and Raman results, it can be concluded that the carbonaceous material conforming the electrodes is glassy carbon, which is widely used as electrode material for electrokinetic applications [56, 57].

Chapter 5

Bidirectional fluid pumping by AC electroosmosis

5.1 Amplitude and frequency dependence of fluid velocity

During each half period of the AC signal, $1/2(f_w)$, opposite electrodes alternate their superficial charge, either from positive to negative or vice versa, in response to the oscillation of the applied polarizing signal. At low frequencies, the electrode polarization frequency is close to the characteristic double-layer relaxation frequency, given by

$$f_{RC} = \frac{(1+\delta)\,\rho_f \lambda_D}{2\pi\varepsilon_f d} = 828 \text{ Hz}, \tag{5.1}$$

where δ is the surface capacitance ratio, ρ_f is the fluid conductivity, λ_D is the Debye length, ε_f is the fluid permittivity and d is the characteristic macroscopic length scale of the system [75–77]. In this case, the adjoining suspended ions interact with the polarized electrode, allowing vortex formation to propel the bulk fluid from the EDL. As the working frequency becomes $f_w \gg f_{RC}$, no electrostatic interactions occur due to an extremely short polarization time, thus vortex formation is completely inhibited. Table 5.1 shows the parameters used to calculate the characteristic double-layer relaxation frequency.

Table 5.1: Set of parameters and corresponding values to determine the characteristic double-layer relaxation frequency.

Parameter	Value	Description
$\varepsilon_f = \varepsilon_0 \varepsilon_r$	6.95×10^{-10} F/m	Fluid permittivity
σ_f	5.5×10^{-4}S/m	Fluid conductivity
$\lambda_D = \sqrt{\frac{\varepsilon_f RT}{2F^2 C_0}}$	128.04 nm	Debye length of the electric double layers
C_s	0.2 F/m^2	Capacitance of the Stern layer (typically used value. See reference [75])
$C_D = \frac{\varepsilon_f}{\lambda_D}$	0.0054 F/m^2	Capacitance of the diffuse layer
$\delta = \frac{C_D}{C_S}$	0.0271	Surface capacitance ratio
d	20 μm	Characteristic macroscopic length scale of the system (width of E_{N}))

Additionally, all devices showed higher fluid velocities for frequencies below 1 kHz at low amplitudes (< 10 V_{PP}), compared to flows observed at 1 kHz at the same amplitudes, which is in good concordance to the estimated relaxation frequency; however, electrolysis and bubble formation was observed for amplitudes above 10 V_{PP}, leading to electrode degradation. The fluid velocity was determined using tracers moving across an electrode-free area of the microchannel, having a reasonable distance to the pumping chambers (>100 μm). In this sense, it was considered that dielectrophoretic effects on the tracers are negligible, thus their movement solely depends on ACEO flow [35].

Flow direction determined by the movement of the tracers is shown in the sequence of images presented in figure 5.1. Here, an electrode asymmetry ratio of 80 μm : 20 μm was used and E_{N} is shown as a reference to indicate forward flow from top to bottom on each frame. A 1 kHz AC signal was applied by sweeping the amplitude from 2 to 20 V_{PP}. In figure 5.1(a) through (c), three tracers are tracked moving towards E_{N}, while others are static due to fouling and adhesion to the substrate. In this experiment, the forward flow is evident from 10 to 14.4 V_{PP}. Then, at 14.6 V_{PP}, tracers' recirculation without net flow can be observed on figure 5.1(d) through (f). Here, tracers 1, 2 and 3, are the farthest from the electrodes and have no participation in the formed vortices, and show only Brownian motion; however, tracers 4 and 5, which are closer to the electrodes, move towards the electrode surface. At this point, forward flow at the electrode surface and reverse flow at the top of the microchannel cancel out each other, thus no net flow is produced. Finally, tracers moving away from the electrode were tracked for signal amplitudes higher than 14.6 V_{PP}, as shown in figure 5.1(g) through (i).

The maximum experimental fluid velocities achieved in forward and reverse regimes, respectively, for the asymmetry ratios (*i*), (*ii*) and (*iii*), over the tested working frequency range (1 kHz $\leq f_w \leq$ 1 MHz) are shown in figure 5.2(a) and (b). Clearly, the highest forward (figure 5.2(a)) and reverse (figure 5.2(b)) velocities are achieved for the lowest working frequencies (1—2 kHz) due to an electrode polarization time larger than the charge relaxation time, and velocities decrease sharply as f_w is increased. For a given device, velocity

decreases as frequency increases for both flow regimes due to the lack of charge interaction between suspended ions and polarized electrode surface. This effect was consistently observed on the three different devices for both forward and reverse flows, as can be seen from figure 5.2(a) and (b), respectively. The velocity ratio of maximum reverse flow to maximum forward flow for devices (*i*), (*ii*) and (*iii*) was 11.82, 11.76 and 13.90, respectively, indicating that fluid velocity difference between reverse and forward fluid movement remains relatively constant, independently of the electrode asymmetry ratio.

The effect of electrode asymmetry ratio on fluid velocity is also visible in figure 5.2(a) and (b), showing that for the tested devices, the lower the asymmetry ratio, the higher the fluid velocities that can be reached. This suggests that as E_{W} is increased, more time is required to create uniform charge distribution on the entire electrode surface, since the electric field is stronger across G_1 than across G_2 because opposite electrodes are closer together. This increases the effective separation between adjacent electrode pairs, hence reducing the driving forces on the bulk fluid due to weak vortex interactions.

Figure 5.2(c) shows the normalized fluid velocity evolution for the electrode systems with three asymmetry ratios in an amplitude range of 0–20 $\mathrm{V_{PP}}$ at 1 kHz. Low applied amplitudes (2–8 $\mathrm{V_{PP}}$) produce an undefined velocity pattern due to undeveloped flow. However, at 10 $\mathrm{V_{PP}}$, a velocity pattern is established, and at 12 $\mathrm{V_{PP}}$, the maximum forward flow regime is reached. The fluid velocity is reduced as the asymmetry ratio increases. The highlighted zone shows the transition from forward to reverse regime as the signal amplitude is increased. This transition occurs between 14 and 16 $\mathrm{V_{PP}}$ for the smaller asymmetry ratio (60 µm : 20 µm) and between 12 and 14 $\mathrm{V_{PP}}$ for larger asymmetry ratios. The same velocity pattern with respect to the asymmetry ratio is observed for the reverse flow as well.

5.2 Effect of microposts integrated onto asymmetric-coplanar electrodes

Fluid velocity for all the tested devices is mapped in figure 5.3, including velocity measurements for planar electrodes (figure 5.3(a–c) for devices (*i*), (*ii*) and (*iii*), respectively), and planar electrodes with HAR microposts (figure 5.3(d–f) for devices (*iv*), (*v*) and (*vi*)). Red and blue colors depict areas of forward and reverse regimes, respectively. Hue intensity indicates the relative magnitude of the velocity.

In contrast to planar electrodes, HAR electrodes (lower row) showed a wider forward flow regime along AC magnitude and frequency, caused by hydrodynamic channeling; however, maximum velocities are lower than for devices with planar electrodes (without posts). Maximum velocities achieved by devices (*iv*), (*v*) and (*vi*) were, respectively, 6.34 µm/s, 9.23 µm/s and 6.02 µm/s in the forward regime; and 79.71 µm/s,

90.66 μm/s and 14.66 μm/s in the reverse regime. These velocities indicate that a higher electrode contact surface with the fluid does not necessarily guarantee a fluid velocity increase. One possible explanation is that closely-spaced posts create a significant drag that retards the propulsion of the flow. Another possibility is that vertically-generated vortices on two facing micropost surfaces (*i.e.*, developed on same electrode finger) collide with each other before completing a full vortex, thus propelling the fluid in the opposite direction. This suggests that micropost separation should be increased to allow complete vortex formation; however, the amount of microposts on the electrode would be reduced in consequence, considerably decreasing the electrode surface area in contact with the fluid for a constant microchannel width.

This effect would also explain the fluid direction switching from reverse to forward in the forward regime (from 4 to 14 V_{PP} and between 1 and 2 kHz, as shown in figure 5.3(d) and (e)), and the eventual fully reverse flow in both forward and reverse regimes at low frequencies (figure 5.3(f)). We have shown that the highest velocity for the tested planar devices is achieved by the lowest asymmetry ratio (*i.e.*, 60 μm : 20 μm) by achieving the largest horizontally-driven vortex formation. However, the short distance between adjacent microposts ($\sim$ 57 μm) and the large height (80 μm) allows vertically-driven vortices to propel fluid at low amplitudes due to the small vortex size required to drive the fluid in the reverse direction, since two facing electrode surfaces contribute to this task. Once the coplanar surfaces become dominant due to a higher horizontally-driven vortex size, the fluid switches to a forward propulsion and continues until reaching the reverse regime. This effect applies for all devices and, as the coplanar surfaces become less dominant with the increase on asymmetry ratio, the vertically-driven vortices become dominant until only reverse flow is achieved at low frequencies.

These results also suggest that HAR microposts can be used to produce fluid velocities of fairly similar magnitudes in forward and reverse directions, yielding symmetric flow, by diminishing reverse flow and amplifying forward flow. For the case of the three asymmetry ratios characterized in this work, the ratio of maximum reverse regime velocity to the maximum forward regime velocity was reduced as the electrode asymmetry ratio increased: 12.55, 9.81, 2.41 for devices (*iv*), (*v*) and (*vi*), respectively, indicating that, as the electrode asymmetry ratio increases, forward and reverse flows become more symmetric, on the expense of a net fluid velocity decrease. This effect can be observed on figure 5.3(f), where red and blue hues have practically the same intensity in some points. This behavior is contrasted to that for coplanar electrodes without posts, where the reverse/forward fluid velocity ratio remained nearly constant.

5.2.1 Effect of Shorter Microposts on Flow Development

On an additional analysis, a set of 40 μm-height microposts was fabricated using the same photomasks that for the HAR microposts; however, this time, an 80 μm PR layer was spin-coated to obtain shorter microposts. This set of microelectrodes was contrasted to planar and 80 μm-height microposts to study the effect of lower surface area of the fluid velocity. For this experiment we set the asymmetry ratio to 20 μm:80 μm.

Velocity test results show that asymmetric coplanar electrodes (*i.e.*, device (*i*)) can develop forward only at the lower frequencies (*e.g.*, 1 and 2 kHz), while for higher frequencies, only reverse flow is developed. Figure 5.4 shows maximum fluid velocities in both, (a) forward and (b) backward directions achieved at different AC frequency conditions, for the three devices. However, as can be seen in Figure 5.4b, the presence of microposts atop of coplanar electrodes precludes the flow inversion, accompanied by the overall reduction in fluid flow (as compared to planar electrode structure). The most pronounced flow inversion is evident for planar electrodes where forward flow velocity is significantly lower than the backflow that takes place after flow inversion. For 40 μm-height posts-containing electrodes, a low-magnitude backward flow is observed only at the lowest frequencies (1, 2 and 10 kHz in Fig 5.4b), whereas a significant forward flow is observed for these electrodes in the entire range of frequencies tested (from 1 to 200 kHz in Figure 5.4a).

Figure 5.5 shows fluid velocity development at 1 kHz with respect to the AC amplitude sweep from 2 to 20 V_{PP}. Here, the higher fluid velocities are achieved at the higher AC amplitudes (i.e. 8 to 20 V_{PP}), in good concordance with the previously presented results. However, it is notable that at the highest AC amplitudes, fluid velocities between devices (*i*) and (*iii*) become comparable in magnitude, possibly meaning that without the action of the planar electrodes' surface, micropost would develop even higher fluid velocities in the forward direction. Interestingly, for device *ii*, whereas fluid velocity is reduced in the reverse regime, flow becomes considerably more symmetrical in magnitude. For this particular case, maximum reverse and forward fluid velocities are 36.61 μm/s and 14.2 μm/s, respecetively, leading to a reverse/forward ratio of 2.57, in contrast to the 10.49 ratio for the asymmectric coplanar electrodes, and the 11.64 ratio for the 80 μm-height micropost. This results suggest that microposts height with respect to the microchannel height plays an important role on the flow symmetry of the micropumps, and has to be taken into consideration on designing application-specific devices, where flow symmetry is more relevant than fluid velocity.

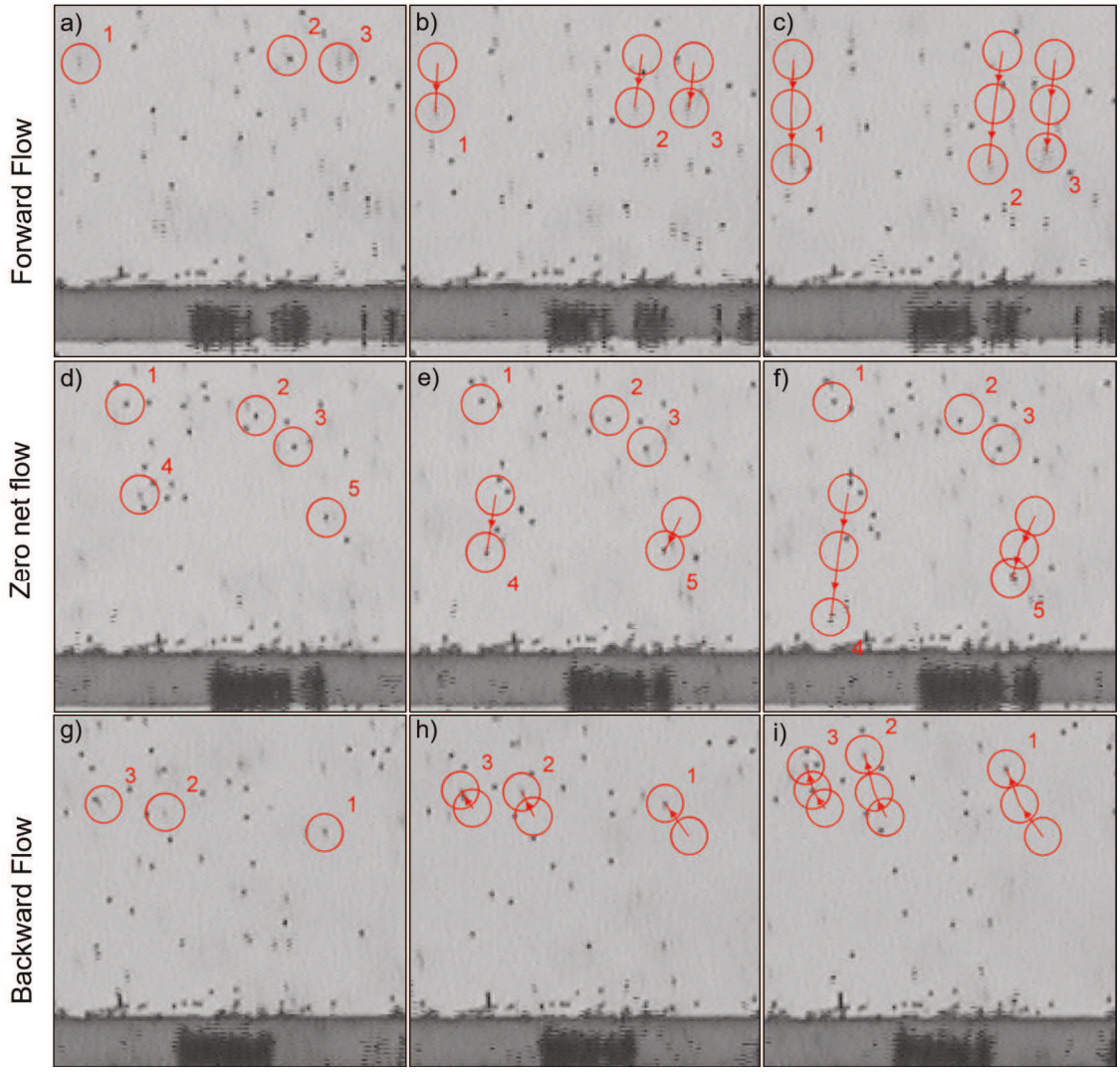

Figure 5.1: Sequential pictures of tracers tracking during three micropump operational stages: (a), (b) and (c) forward flow; (d), (e) and (f) recirculation of tracers with zero net flow; and (g), (h) and (i) reverse flow. Electrode EN is shown in all pictures, indicating forward flow as tracers moving from top to bottom of the frame.

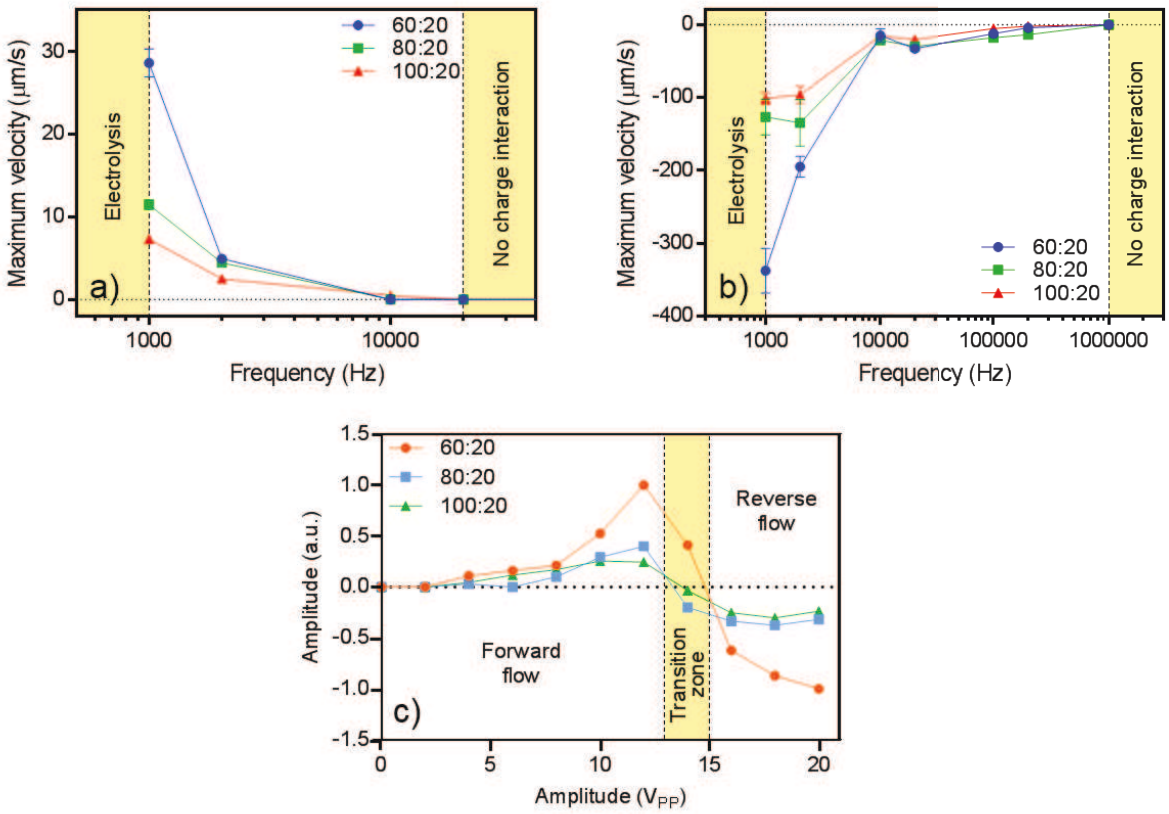

Figure 5.2: (a) Forward and (b) reverse flow velocity measurements for devices (i), (ii) and (iii), and (c) Normalized fluid velocity evolution for the three tested electrode asymmetry ratios. Forward and reverse flows at 1 kHz and amplitudes from 0 to 20 VPP. Highlighted area shows transition from forward to reverse flow as the signal amplitude increases.

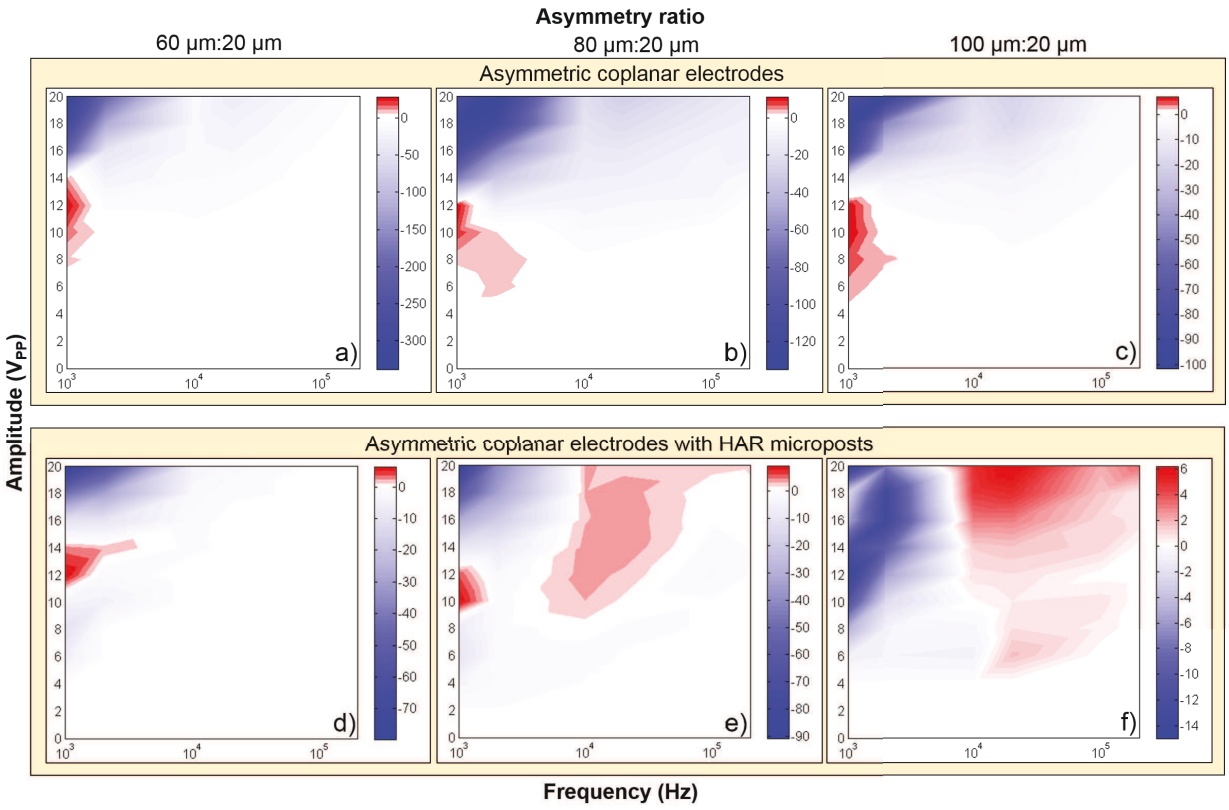

Figure 5.3: Color maps of measured fluid velocity for asymmetric-coplanar electrodes: (a), (b) and (c) for devices (*i*), (*ii*) and (*iii*), respectively; and asymmetric-coplanar electrodes with HAR microposts: (d), (e) and (f) for devices (*iv*), (*v*) and (*vi*), depending on applied AC magnitudes and frequencies. Red and blue colors indicate forward and reverse flow regimes, respectively; intensity of the hue indicates the relative magnitude of the flow velocity.

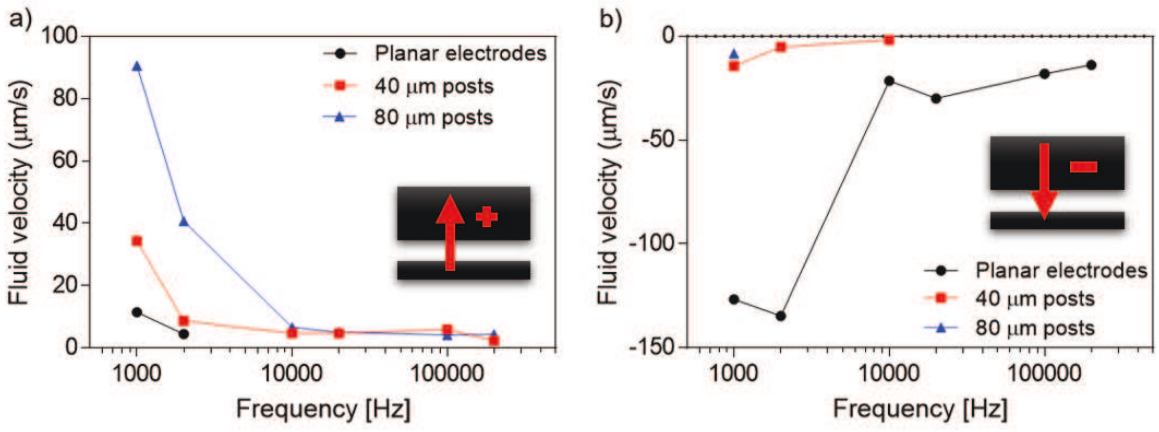

Figure 5.4: Maximum (a) forward and (b) backward fluid velocities for frequency range from 1 to 200 kHz for planar electrodes, planar electrodes with 40 µm-height microposts and planar electrodes with 80 µm-height microposts.

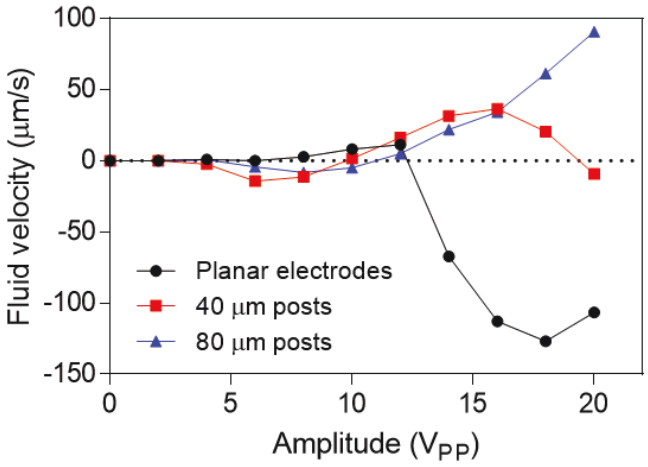

Figure 5.5: Fluid velocity development with respect to the AC amplitude sweep at 1 kHz for planar electrodes, planar electrodes with 40 µm-height microposts and planar electrodes with 80 µm-height microposts.

Chapter 6

Conclusions and future work

In this work, we presented results on bidirectional fluid pumping using AC electroosmosis due to hydrodynamic channeling to control flow reversal in a microchannel using 2D and 3D glassy carbon electrodes. For the first stage of this work, we carried out a Finite Element analysis to qualitatively contrast fluid velocity for different electrode geometries, including asymmetric coplanar, traveling wave and 3D geometries, to then study in more depth the flow development using asymmetric coplanar geometry, which is the implemented geometry for experimental tests.

For the qualitative study, the three AC electroosmotic micropumps were modeled by solving the Poisson-Nernst-Planck-Navier-Stokes set of equations. The lowest fluid velocity is achieved by the asymmetric coplanar electrode array; the traveling wave electrode array achieves one order of magnitude higher than the asymmetric co-planar array, and the 3D electrode array is the configuration with the highest fluid flow. Both, the asymmetric co-planar array and the 3D array of electrodes generate a small back-flow that reduces the overall performance of the micropump, while the traveling wave array of electrodes preserve a positive flow along all the applied signal cycles. However, the chosen electrode geometry was the asymmetric coplanar array, since fabrication complexity is considerably lower that the other two geometries.

The Carbon-MEMS fabrication process allows for the efficient fabrication of glassy carbon high-surface area structures which otherwise are difficult and/or expensive to make with other materials and fabrication processes. In this study we demonstrated that asymmetric coplanar electrodes develop the higher fluid velocities when contrasted to high surface area structures. However, the implementation of microposts as vertical extensions of planar electrodes, while leading to some fluid velocity decrease, may be useful in situations where flow reversal is not wanted.

Regargin expetimental tests, from the three asymmetry ratios evaluated in this study, the smallest ratio

(60 μm : 20 μm) produced the highest fluid velocity, and velocity magnitude decreased as the electrode pairs' asymmetry increased. The use of high-aspect-ratio microposts leads to a reduction of the net fluid velocity for both, forward and reverse regimes; however, a trend for symmetric velocities was noticed as the electrode asymmetry ratio increased, suggesting that microposts can be used if nearly identical velocity profiles for forward and reverse fluid movements are desirable.

Furthermore, we believe that the optimization of the micropost separation developed along the surface of the planar structures would lead to comparable velocities in both forward and backward directions. This has a great potential in applications where tunable back and forth pumping is required. Microposts can also be used as blockage structure for microfluidic mixing, commonly difficult to achieve at small Reynolds numbers characteristic of the flow in microchannels.

ACEO pumping represents a potential solution for the development of LoC-integrated fluid-driving mechanisms as it offers an easy on-chip integration, multiple fluid pumping chambers on a single microfluidic system, low power consumption, low fabrication costs, and bidirectional fluid pumping as demonstrated in the present work. Further advances of AC electroosmosis pumping can be gained by utilizing more conductive electrode materials as well as optimized electrode geometry.

6.1 Related Publications

1. Vázquez-Piñón, M., Pramanick, B., Ortega-Gama, F.G., Kulinsky, L., Pérez-González, V.H., Madou, M., Hwang, H. & Martínez-Chapa, S.O. (2018). Hydrodynamic channeling as a controlled flow reversal mechanism for bidirectional AC electroosmotic pumping using glassy carbon microelectrode arrays. *Journal of Micromechanics and Microengineering*. Accepted for publication.

2. Vázquez-Piñón, M., Hwang, H., Kulinsky, L., Madou, M. & Martínez-Chapa, S.O. (2018). Effect of carbon microposts integrated onto asymmetric electrodes for AC electroosmotic pumping. *Journal of Micro and Nano Manufacturing*. In press.

3. Vázquez-Piñón, M., Cárdenas-Benítez, B., Pramanick, B., Pérez-González, V.H., Madou, M., Martínez-Chapa, S.O. & Hwang, H. (2017). Direct current-induced breakdown to enhance reproducibility and performance of carbon-based interdigitated electrode arrays for AC electroosmotic micropumps. *Sensors and Actuators A: Physical*, 262, 10-17.

4. Vázquez-Piñón, M., Kulinsky, L., Madou, M., & Martínez-Chapa, S.O. (2018). Effect of carbon microposts integrated onto asymmetric electrodes for AC electroosmotic pumping. *World Congress on*

Micro and Nano Manufacturing, Portoroz, SI, September 18–20, 2018.

5. Vázquez-Piñón, M., Cárdenas-Benítez, B., Pramanick, B., Pérez-González, V.H., Madou, M., Martínez-Chapa, S.O., & Hwang, H.L. (2018). Residual Carbon Breakdown by Joule Heating in C-MEMS Interdigitated Electrode Arrays. *International Conference on Expanding Frontiers of Carbon MEMS*, San Diego, CA, USA, June 10–12, 2018.

6. Vázquez-Piñón, M., Kulinsky, L., Pérez-González, V.H., Madou, M., Martínez-Chapa, S.O. & Hwang, H. (2016). Effect of interdigitated electrode asymmetry on performance of carbon-based AC electroosmotic micropumps. *Proceedings of the 2016 AIChE Annual Meeting*, San Francisco, CA, USA, November 13-18, 2016.

7. Vázquez-Piñón, M., Pérez-González, V.H., Camacho-León, S., Gallo-Villanueva, R., Madou, M., & Martínez-Chapa, S.O. (2014). Qualitative Study of AC Electroosmotic Micropumps by Computational Modeling of Non-Equilibrium Electrokinetics. *Proceedings of the 2014 AIChE Annual Meeting*, Atlanta, GA, USA, November 16-21, 2014.

Appendices

Appendix A

Joule-heating treatment for C-MEMS microelectrode arrays

A B S T R A C T

The conventional C-MEMS fabrication process often yields undesired carbon residues that reduce the reproducibility and performance of final structures by establishing unwanted electrical connections. In this chapter it is proposed a straightforward method based on the application of a low direct current (DC) to effectively remove undesired electrical connections. The DC bias causes the breakdown and removal of short-circuiting carbon residues due to Joule heating, resulting in significantly enhanced performance and reproducibility of the final structures.

We fabricated carbon-based asymmetric coplanar interdigitated electrode arrays (IDEAs) for alternating current electroosmotic (ACEO) micropumps using the conventional Carbon-MEMS process. By scanning electron microscopy (SEM); Raman, energy dispersive X-ray (EDX) spectroscopies; four-point probe resistance measurements; and the combination of ion-beam etching and X-ray photoelectron spectroscopy (XPS), we confirmed the presence of residual carbon in the gaps of the IDEAs and established its deleterious effect on electrical properties of the structures and their performance as electrodes in micropumps.

A computational study was also conducted to estimate the temperature increase due to the DC bias applied across a thin residual carbon. Experimentally, we found that the DC-treated IDEAs exhibited more than double the fluid velocity in ACEO pumping compared to untreated devices; and also, the coefficient of variation of the fluid velocity for the DC-treated ACEO micropumps was significantly smaller than that for the untreated ones. This simple and easy-to-implement method can substantially improve the yield

of Carbon-MEMS manufacturing, leading to a highly reproducible production of high performance carbon electronic circuits and microstructures.

A.1 Introduction

In carbon-microelectromechanical systems (C-MEMS), polymer microstructures patterned by photolithography on a substrate are carbonized at high temperatures (900–1100°C) in an oxygenfree environment. During the process, most of the non-carbon atoms from the polymer are released to the ambient, resulting in a shrunken and electrically conductive glassy carbon (GC) material. This straightforward and cost-effective manufacturing process has demonstrated to be versatile enough to enable a very extensive variety of carbon based micro- and nanostructures, including interdigitated electrode arrays (IDEAs) [78], suspended nanowires and nanomeshes [79, 80], cantilever beams [81], high surface area porous carbon [82], C-MEMS-derived three dimensional graphene structures [83], and high-aspect ratio microposts [84]. Owing to GC unique material properties—e.g., high electric conductivity, chemical stability and biocompatibility—C-MEMS have found several applications, such as electrochemical sensing [85], electrokinetic pumping [53], particle manipulation [86, 87], and triboelectric nano-generation [60].

One key application of C-MEMS IDEAs is alternating-current electroosmotic (ACEO) pumping, used to drive electrolytic fluids without the need of moving parts and in a controlled fashion. Here, when an electric potential difference is applied across the electrodes, the electrode polarization establishes an electric field which draws suspended ions from the electrolyte towards the electrode surface, resulting in an induced electric double layer (EDL) at the electrode-electrolyte interface. The ions, in turn, drag fluid molecules along by viscous forces—Stokes' law. The asymmetric co-planar array is the most commonly used electrode geometry in ACEO pumps due to their low fabrication complexity and high performance [38, 88]. In this geometry, the electrode width of one comb, EN, is narrower than the electrode width of the opposite comb, EW, as shown in Fig. A.1(a). When an AC electric potential bias is applied across the electrode set, the back and forth movement of fluid molecules creates vortices on the surface of the electrodes. Due to the electrodes asymmetry, these vortices differ in size, causing a net fluid flow in the direction of the larger vortex, as depicted in Fig. A.1(b). The ACEO flow is mainly determined by the geometry of the electrodes and by the frequency and amplitude of the applied signal [39].

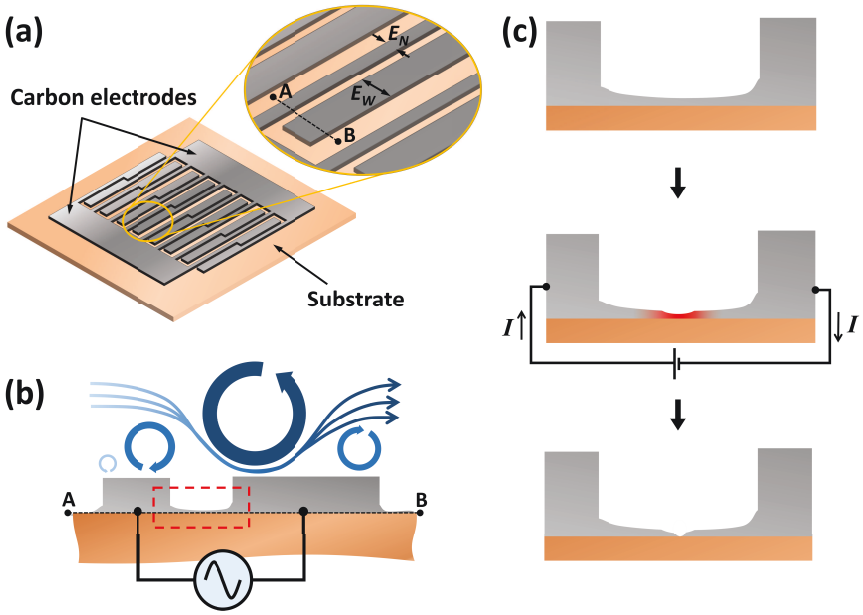

Figure A.1: Schematic diagram of carbon-based interdigitated electrode arrays (IDEAs) for AC electro-osmotic (ACEO) pumping. (a) Carbon-based asymmetric coplanar IDEAs, in which the width of one electrode, EN, is narrower than the width of the opposite electrode, EW. (b) ACEO flow induced by the carbon IDEAs. (c) A low direct current breaks the residual carbon layers in the gap between two electrodes, resulting in highly reproducible fabrication of carbon electrodes-based ACEO micropumps.

IDEAs have been used not only for pumping fluids, but also for a variety of biotechnology applications including fluid mixing [88]; concentration of nanoparticles [89], DNA molecules [37], and microalgae [54]; and immunoreactions for detection of biomarkers [90]. Commonly, ACEO micropumps and other microstructures are fabricated using noble metals as electrode material [38]. This practice often yields high manufacturing costs and requires the use of specialized fabrication facilities, which are not commonly available. For these reasons, C-MEMS-based microstructures are currently under exploration, not only as a potential alternative to metallic electrodes for bio-applications [91], but also as an electrochemically-functionalized substrate for biosensors, biofuel cells and cell culture [92], among others.

The formation of thin residual carbon layers has been one of well-known problems of the C-MEMS fabrication technology. The carbon residues often connect adjacent electrodes or disturb the structures, thus lower the reproducibility and performances of the C-MEMS devices [69]. This particularly affects the performances of carbon electronic devices, such as electrochemical sensors and electrokinetic actuators, by shunting the electrodes. Furthermore, as the feature size of carbon structures decrease, shunt currents become more significant in the overall electric circuit. For the case of IDEAs, such as those employed in ACEO micropumps, the presence of residual carbon in gaps between adjacent electrodes decreases the electrical

resistance between opposite electrodes, thus affecting the electric field magnitude necessary to induce the fluidic motion, reducing the performances of these C-MEMS devices in consequence.

Residual carbon found in devices fabricated using the conventional C-MEMS process has at least three possible causes: (i) residual SU-8 photoresist due to improper development; (ii) diffusion of carbon atoms onto the substrate during pyrolysis [83, 93]; or (iii) dust contamination during the fabrication process. To remove these residues, the use of pressurized air to blow them away was initially proposed as a quick solution, although there is a latent risk of detaching the complete GC structure [69]. Then, an oxygen plasma treatment was tried to dry etch these residues [86]; however, this method has shown to be effective only for extremely thin carbon layers [53, 93]. Although efforts have been previously made to characterize and optimize many fabrication conditions for generation of GC [56], not enough attention has been directed to evaluate and effectively solve the problems due to the residual carbon.

In this work, we propose a new and straightforward method to remove shunts created by residual carbon layers in C-MEMS devices, by applying a low DC-bias treatment, which causes the material breakdown by means of Joule heating due to the high current density distribution along the residual carbon layers. This current-induced breakdown has been widely used to characterize different carbon allotropes in the semiconductor industry; for example, to evaluate the current carrying capacity of different carbon-based interconnects, such as nanotubes [94], nanoribbons [95] and nanofibers [96]; and also to test resistors [97] and transistors [98] that could help in further miniaturization of microelectronics circuits.

To evaluate the applicability of this technique in our C-MEMS devices, we followed the standard procedure to fabricate asymmetric coplanar GC IDEAs, as those depicted in Fig. A.1(a). The resulting structures were characterized to endorse the presence of residual carbon at undesired locations—e.g. the electrode gaps—using scanning electron microscopy (SEM), and Raman and energy-dispersive X-ray (EDX) spectroscopies. To estimate the thickness of the residual films, a depth profiling analysis was carried out using ion-beam etching combined with X-ray photoelectron spectroscopy (XPS). The proposed DC treatment was then applied for residual carbon breakdown and removal of shunts on the fabricated devices, as depicted in Fig. A.1(c). Finally, for a quantitative assessment of this technique, electrical resistance and fluid pumping velocities were measured for devices before and after the DC treatment. We believe that this technique will provide a straightforward solution to address the unavoidable issues related to residual carbon layers in the C-MEMS process, resulting in enhanced performance and reproducibility of carbon electrode-based devices and other electrically-driven microsystems.

A.2 Materials and methods

A.2.1 Fabrication of carbon IDEAs

Asymmetric coplanar IDEAs with a thickness of 1.5 um were fabricated by standard photolithography in a class 1000 cleanroom at controlled 22°C and 38.4% relative humidity, followed by pyrolysis. The narrow electrode is E_N = 20 μm-width, while the wide electrode is E_W = 100 μm-width. Each pair of electrodes has an inner separation of G_1 = 20 μm and each pair is separated by G_2 = 100 μm from an adjacent pair. To pattern the polymer precursor microstructures, a silicon wafer with a 500-nm-thick SiO2 layer was used as substrate (NOEL Technologies, Campbell, CA, USA). Negative photoresist SU-8 2002 (MicroChem Corp, MA, USA) was spin coated on the substrate surface at 500 rpm for 10 s and then at 1000 rpm for 30 s, to a final thickness of 3 μm, followed by a soft bake on a hot plate at 95°C for 2 min. The photoresist was then UV-patterned to an energy of 90 mJ/cm^2 through a film photomask to selectively crosslink the interdigitated electrode structures. After a post-exposure bake at 95°C for 2 min, the processed wafer was immersed in SU-8 developer solution (MicroChem Corp, MA, USA) for 1 min to remove uncrosslinked photoresist. Finally, developer remains were rinsed off with isopropyl alcohol and deionized water, and the wafer was blow-dried with N_2.

Pyrolysis was carried out in an open-ended tube furnace (Mini #40, R.D. Webb Company, Inc., Natick, MA, USA) in a N_2 environment in a three-step process to a maximum pyrolysis temperature of 900°C and a gas flow rate of 2000 sccm, following the temperature profile previously reported by our group [56]. The pyrolysis results in a considerable isotropic shrinkage of the original SU-8 structures yielding the targeted IDEAs height of 1.5 μm. Fig. A.2 shows a scanning electron microscopy (SEM) image of the resulting asymmetric coplanar carbon electrodes.

A.2.2 Device characterization

Physical characterization of the devices was carried out to confirm the presence of residual carbon layers across the electrode gaps, G_1 and G_2. First, the IDEAs were visually examined by SEM (EVO MA25, Carl Zeiss AG, Oberkochen, DE). Then, to determine whether the undesired features in the SEM images are residual carbon, an elemental analysis was carried out by EDX at three different device locations: (*i*) carbon electrodes, (*ii*) electrodes gap, and (*iii*) bare SiO_2 substrate. The atomic percentage of carbon, silicon and oxygen was quantified in the EDX analysis. Furthermore, Raman spectroscopy (inVia Raman microscope, Renishaw, UK) was used to determine the graphitic (sp2) and disordered carbon (sp3) contents of the residual layers in the electrode gap. Raman spectra were obtained using 514 nm Ar laser excitation (Modu-Laser,

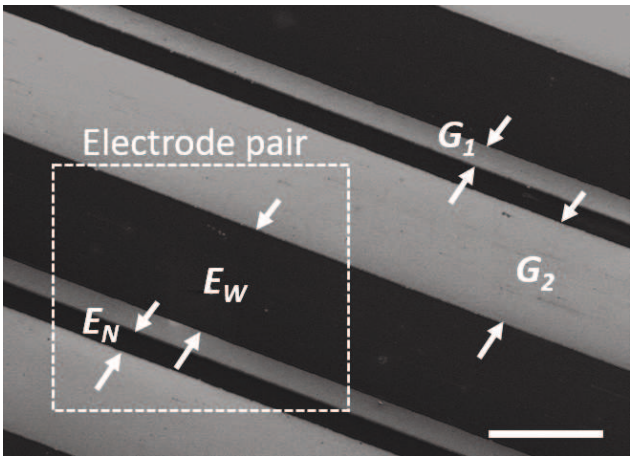

Figure A.2: SEM image of the fabricated carbon electrodes for AC electroosmotic pumping. Geometric parameters for each electrode pair are also indicated: the width of narrow electrode, $E_N = 20$ µm, the width of wide electrode, $E_W = 100$ µm, the gap distance between E_N and E_W, $G_1 = 20$ µm, and the gap distance between the electrode pairs, $G_2 = 100$ µm. Scale bar = 100 µm

LLC, Centerville, UT, USA) at the three mentioned locations. The measured Raman scattering signals from three different surrounding points were averaged for each location. The electrical resistance of the circuit was measured with a digital multimeter (5491A, BK Precision, Yorba Linda, CA, USA) on untreated devices to determine the characteristic resistance range of the residual carbon material.

To determine the thickness of the residual carbon layer, an Ar ion beam with a spot size of 100 um and an etch rate of 0.51 nm/s was used to etch the residual carbon layers of several devices with different residual carbon resistance values, ranging between 4 kΩ and 11 MΩ. Surface analyses were carried out by means of XPS at the un-etched residual carbon surface and at an etching depth of 4.2 nm.

Once the presence of a carbon residual layer at the electrodes gap was verified and its thickness was determined, the un-etched devices were treated with a 4 mA DC applied through the electrode combs using a high voltage sequencer (HVS448 6000D, LabSmith, Livermore, CA, USA) on 60 s time spans. The resistance of the devices was measured after each time span and the process was repeated until open circuit was achieved.

A.2.3 Finite element analysis

A computational model was built using COMSOL Multiphysics (COMSOL, Inc., Stockholm, SE) to estimate the current density and temperature increase across the residual carbon layer due to the applied DC. The geometry employed in the model consists of a 2D representation of one pair of electrodes with a thin carbon layer in between, as shown in Fig. A.1(c). This glassy carbon film was set to be 30 nm-thick, 20 µm-long (inner electrode separation, G_1), and 10 µm-wide, defined by the out-of-plane attribute for a 2D model in the software, d_z. For the chosen geometry, the film resistance was taken to be 200 kΩ, fitting in the measured

resistance range of the fabricated devices. Additionally, a 500 nm-thick SiO_2 layer on the Si substrate was assumed. For this geometry, the temperature distribution T was solved using the time-dependent heat equation:

$$\rho_c C_p \frac{\partial T(\mathbf{r},t)}{\partial t} = \nabla(\kappa \nabla T(\mathbf{r},t)) + \frac{\mathbf{J}^2}{\sigma} - Q(\mathbf{r},t) \tag{A.1}$$

where ρ_c is the glassy carbon density, C_p is the specific heat to a constant pressure, $\mathbf{r}$ is the position, κ is the thermal conductivity of the heated material (6.3 $\mathrm{W/m \cdot K}$ for glassy carbon [99]), $\sigma = 100\mathrm{S/cm}$ is the electrical conductivity [100], Q is the heat loss term defined by convective and radiative heat losses, and $\mathbf{J}$ is the local electric current density. For the convective heat transfer coefficient in air, the standard value of 50 $\mathrm{W/m^2K}$ was used, and for radiative losses, an emissivity of 0.820 [101]. Finally, to define $\mathbf{J}$, an input current of 4 mA was assumed, matching the experimental value.

A.2.4 Experimental setup for ACEO micropumps

To test the performance of ACEO micropumps before and after DC treatment, 100 um-height PDMS microchannels were fabricated using standard soft lithography. The PDMS mold was bonded onto the C-MEMS device using a 2-min air plasma treatment. Copper wires were soldered to the electrode combs and the contact zones were covered with commercially-available epoxy resin to permanently seal the electric joint. After filling the PDMS microchannels with bi-distilled water (buffer = 1.2 S/cm) containing 1 um-diameter polystyrene microbeads as tracer particles, a voltage amplitude sweep from 1 to 12 V_{PP} at 1 kHz was applied to the electrodes to induce ACEO flow. For each voltage step, a 30-s video was recorded once the flow was fully developed.

The mean velocity of the microbeads (assumed as the velocity of the fluid) was measured using particle-tracking software (ImageJ, National Institutes of Health, Bethesda, MD, USA). For this purpose, the particles velocity was measured on an electrode-free area of the microchannel to avoid contributions of the local vortices and only considering the movement of the bulk fluid. The microscope was focused approximately halfway the microchannel height, where the particles showed a stable horizontal movement. A demonstration video showing the generated electroosmotic flow is available in the supplementary material section.

A.3 Results and discussion

The SEM image in Fig. A.3(a) shows a residual layer of material across the gap of IDEAs. For a better comparison, carbon microposts were additionally developed on top of the planar electrodes by the second

photolithographic patterning step and then peeled off using a micromanipulator (Model 525, Micromanipulator, Carson City, NA, USA) to expose the SiO_2 substrate and contrast it against residual carbon. When using a backscattered electron (BSE) detector for SEM imaging, as in the case of Fig. A.3(a), electrodes and microposts are darker than the silicon dioxide surface due to the lower atomic number of carbon compared to silicon [102]—post sidewalls are charged due to the electron beam incidence angle. An intensity analysis across the electrode gap was measured along the profile shown in Fig. A.3(a) to differentiate between SiO_2 and residual carbon. The intensity plot in Fig. A.3(b) shows a clear intensity drop across the electrode gap, suggesting a material layer with lower atomic number compared to the SiO_2 substrate, such as carbon. Carbon layers in the gap might be formed by carbon diffusion during pyrolysis or by improper development; for this specific case, dust contamination is unlikely to be the cause due to the uniformity of the residue.

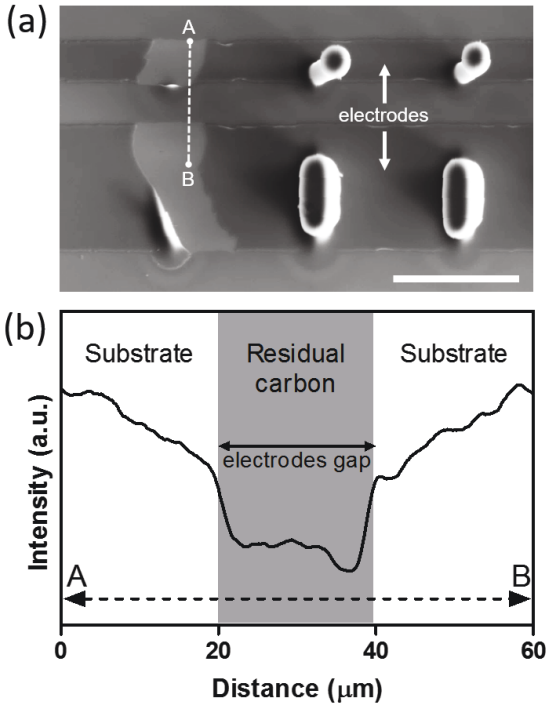

Figure A.3: Physical characterization of interdigitated electrodes and carbon residues. (a) Backscattered-electron image showing carbon electrodes with microposts, residual carbon, and SiO_2 substrate. The dashed line between A and B marks denote the line profile for the intensity analysis. (b) The intensity profile along A–B in (a), where a clear intensity drop is noticed across the electrodes gap. Scale bar = 100 μm

For elemental analysis, the measurement locations are marked on the SEM image in Fig. A.4(a), where (i) the carbon electrode, (ii) residual carbon across the electrodes gap, and (iii) the bare SiO_2 substrate (from the peeled-off microposts) are shown. The EDX spectra for the corresponding locations are shown in Figs. A.4(b) and (c). As expected, a high-count carbon peak was found for the electrodes, representing 54.1% of

the atomic percentage (27.9% silicon and 18% oxygen). Across the small electrode gap, presence of carbon atoms was also detected, although the peak is considerably lower than for the electrodes. In this case, the carbon atomic percentage is 17%, whereas for silicon it is 40.8% and it is 42.2% for oxygen, suggesting a thin residual carbon layer in the electrode gaps. Finally, on the bare SiO_2 substrate, a carbon atomic percentage of 4.6% was found, and a 42.9% for silicon and 47.9% for oxygen. The presence of carbon on the bare substrate could be due to a small amount of carbon atoms diffused onto the SiO_2 caused by the high temperatures reached during pyrolysis. Fig. A.4(c) shows a close view of the carbon peaks from Fig. A.4(b), where a considerable decrease in the amplitude of carbon peak (at 0.277 keV) is observed as the spectra move from the (i) carbon electrode to (ii) residual carbon, and to (iii) the SiO_2 substrate, where it becomes essentially null. Silicon peak amplitudes (at 1.739 keV) are constant throughout the three locations, whereas the oxygen presence (at 0.525 keV) increases from (i) through (iii), as the amount of carbon is reduced, meaning that more SiO2 is detected instead.

Raman spectroscopy analysis was carried out on the same device locations shown in Fig. A.4(a). Particularly at the electrode gap, three measurements were taken across the gap width and averaged for a comprehensive characterization. The characteristic D (1350 cm^{-1}) and G (1590 cm^{-1}) bands, indicating the presence of amorphous (sp^3) and graphitic (sp^2) carbon crystallite formations, respectively, were detected not only at the electrodes, but also across the electrodes gap, as shown in Fig. A.5. The intensity ratio between the D and G bands, I_D/I_G, close to 1, and a broad D-band suggest an equivalent amount of amorphous and graphitic contents in both locations, which is in good agreement with previously reported studies on pyrolytic carbon using SU-8 as a polymeric precursor [103]. On the SiO_2 substrate, no presence of D or G bands was observed.

XPS analysis of the devices with different electrical resistance was also conducted. Here, an Ar-ion beam was utilized to investigate changes in the chemical composition across the depth of the residual carbon layer. Results before and after etching to a depth of 4.2 nm are compared in Fig. A.6. The results of the four devices were consistent. O1s (532.9 eV) and Si2p (103.5 eV) peaks were found, corresponding to SiO2, in all cases. C1s peaks are present for all the four devices at a binding energy of 284 eV before etching. After etching, the peak corresponding to carbon became negligible, meaning that the residual carbon layer was removed at an etching depth of 4.2 nm or less. Small C1s peaks remained for some devices (not shown in Fig. A.6), suggesting that the residual carbon is non-uniform along different devices. A possible reason for this is an uneven spincoated photoresist layer during photolithography, possibly caused by the position of those specific devices on the wafer, even though the manufacturer recommended fabrication parameters were followed. Surface analyses were carried out for further etching depths, but no measurable carbon peak

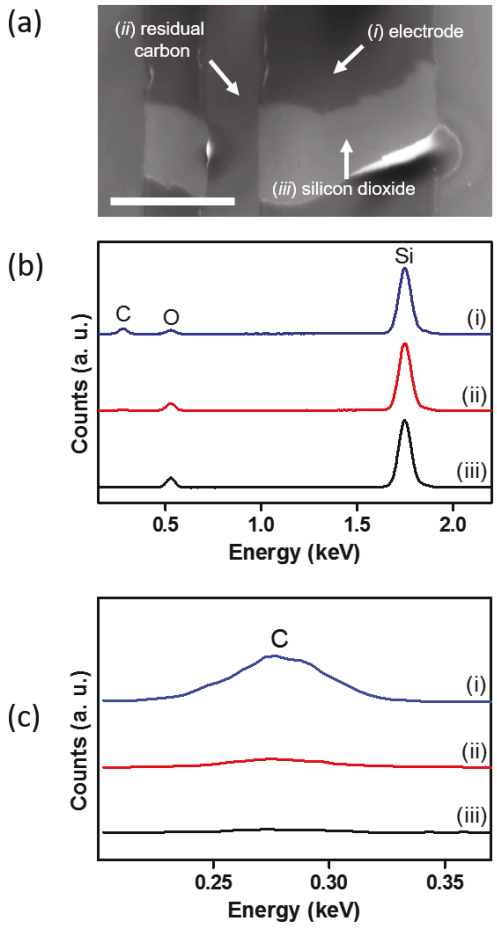

Figure A.4: EDX spectrometry analysis at different locations of the interdigitated electrode arrays: (i) carbon electrode, (ii) residual carbon layer and (iii) bare SiO_2 substrate. (a) SEM image of locations used for elemental analysis. (b) EDX spectra showing peaks corresponding to carbon, oxygen, and silicon atoms, measured at three different locations. (c) Close-up view of a peak corresponding to carbon in (b). Scale bar = 50 µm

changes were observed.

As identified by EDX, Raman and XPS analyses, the carbon residues shunt the electrodes resulting in a finite-resistance electric circuit, as depicted in Fig. A.1(b). These observations verify previous findings that residual carbon layers are formed during the C-MEMS fabrication process and interfere with the normal operation of carbon electronic circuits [53, 69, 86, 93].

Simulation results shown in Fig. A.7 indicate that with the given geometry and an applied direct current of 4 mA, the temperature of the residual carbon layer quickly reaches the maximum temperature of 1660.6 K, which is higher than the oxidation temperature of carbon under atmospheric pressure conditions in air (1200 K to 1600 K) [104], due to the high current density (1.33×10^6 A/cm^2). Fig. A.7(a) and (b) show the cross-sectional geometry of the electrodes gap used for the finite element analysis, and the temperature

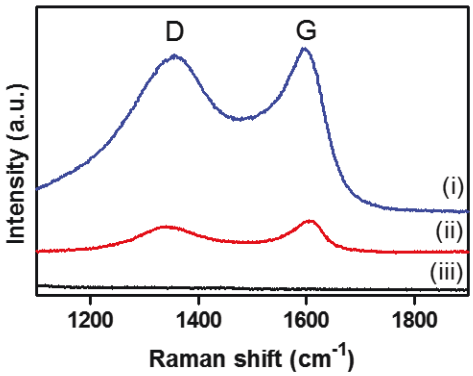

Figure A.5: D (1350 cm^{-1}) and G (1590 cm^{-1}) bands from Raman spectroscopy analysis at three different device locations: (i) carbon electrode, (ii) residual carbon layer, and (iii) SiO_2 substrate.

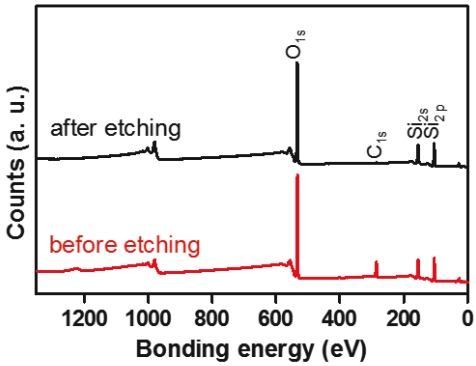

Figure A.6: XPS surface analysis before and after etching a residual carbon film. (i) unetched surface and (ii) 4.2 nm etch depth.

profiles for different time spans after the application of DC at room temperature, respectively. Our model indicates that the maximum temperature is reached within 1 μs after the current is applied, as shown in Fig. A.7(c). The temperature obtained from the model can be established from Eq. (A.1), where the Joule heating term, $\mathbf{J}^2/\sigma$, is directly related to the current density of the residual carbon layer. Since the magnitude of $\mathbf{J}$ is inversely proportional to the available cross-sectional area, which is defined by the nanoscale thickness of the residual carbon layer, t, the heat generation term will grow as $\sim 1/t^2$, resulting in the extreme temperatures reached in the thin carbon film. Particularly, it was found that for nanometric carbon films, current density limits are in the order of 10^6 to 10^8 A/cm^2, which is close to the limit current density of carbon reported elsewhere [105]. However, it is likely that electrical shunts are open-circuited even at a lower current density since intrinsic defects and grain quality of the carbon structure have an impact on the heat transport efficiency and, consequently, on its maximum current density capacity [106]. In our case, the material characterization suggests high content of amorphous carbon at the electrode gaps (See Fig. A.5), meaning decreased current

capacity with respect to graphitic crystallites. In practice, it would take much longer to breakdown all the short circuit points, which are non-uniformly distributed over the complete device area, thus we applied the DC more than 60 s until open circuits were obtained.

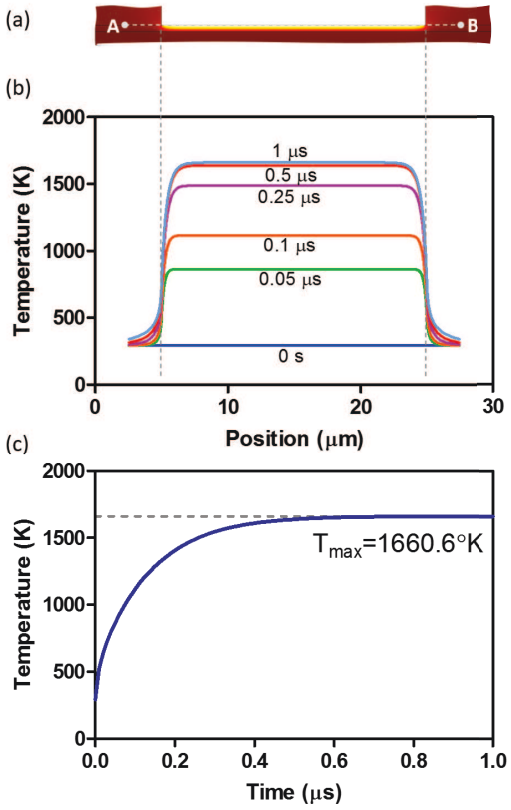

Figure A.7: Finite element analysis of direct current (DC)-induced heating. (a) Model geometry of a 30 nm-thick residual carbon layer on the electrode gap. (b) Temperature profiles at different time spans of the DC treatment at room temperature (273 K). (c) Temporal temperature variation at the center of the residual carbon layer

We measured the electrical resistance of 33 carbon IDEAs fabricated under the same conditions, and results are shown in Fig. A.8. Surprisingly, only 9 of 33 electrodes (27%) exhibited the desired open circuit resistance. In other words, almost three quarters of the fabricated devices revealed shunts caused by residual carbon. Of the 33 samples, 5 (15%) showed resistances below 100 kΩ. To induce open circuits for those devices, direct current was applied for at least 3 min. The wide resistance range can be attributed to the particular quantity of amorphous carbon for each device, which is unpredictable during fabrication.

The performance of ACEO micropumps was experimentally evaluated. We used four devices with different resistance values before the DC treatment: 21.5 kΩ, 236 kΩ, 3.3 MΩ, and infinite resistance (open circuit). The first three devices were treated with a 4 mA DC, and after the treatment, all exhibited infinite resistance,

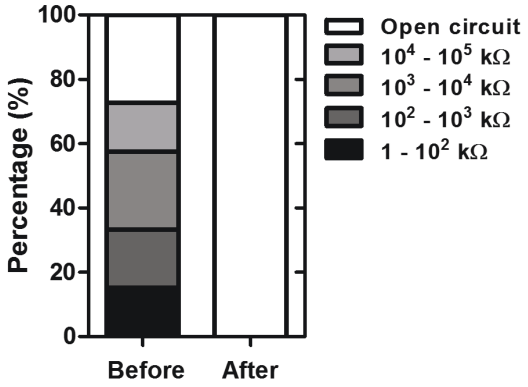

Figure A.8: Change in electrical resistance of the IDEAs before and after the direct current treatment.

meaning that the carbon layer was broken at a random location. The mean maximum flow velocity for the untreated devices was 12.51 μm/s, achieved with an AC signal of 12 V_{PP} at 1 kHz; whereas that of the DC-treated devices was 29.03 μm/s under the same conditions, as shown in Fig. A.9(a). We also calculated the device-to-device variation in the ACEO fluid velocity to quantify the reproducibility of the devices and the results are shown in Fig. A.9(b). The mean coefficient of variation (CV) of the DC-treated devices was 0.24, while that of the untreated devices with short circuits was 0.92. These experimental results show that the DC-induced breakdown of residual carbon layers is a keystone method to improve the performance and reproducibility of C-MEMS IDEAs.

A.4 Conclusions

Residual carbon layers inducing undesired electrical connections between adjacent electrodes have been one of the critical issues in C-MEMS. Simple air blowing and plasma etching have been proposed to address this issue, but the efficiency of these methods have not been quantitatively evaluated, and also the integrity of the carbon structures might be affected with these approaches. In the current contribution, a low DC-bias treatment is proposed as a novel approach to break down undesired electrical shunts due to residual carbon layers formed in the conventional C-MEMS process. The direct current applied through the electrode combs generates a high current density across the residual layers due to their nanometric thicknesses, inducing dramatic increase of temperature, leading to carbon oxidation. The amorphous carbon content of each device limits the maximum current density capacity of the material, which might cause open circuits even at lower temperatures. The breakdown of material occurs at localized regions of the carbon residual layer where the maximum current density is achieved, which not necessarily occurs half-way of the gap, but is mostly defined

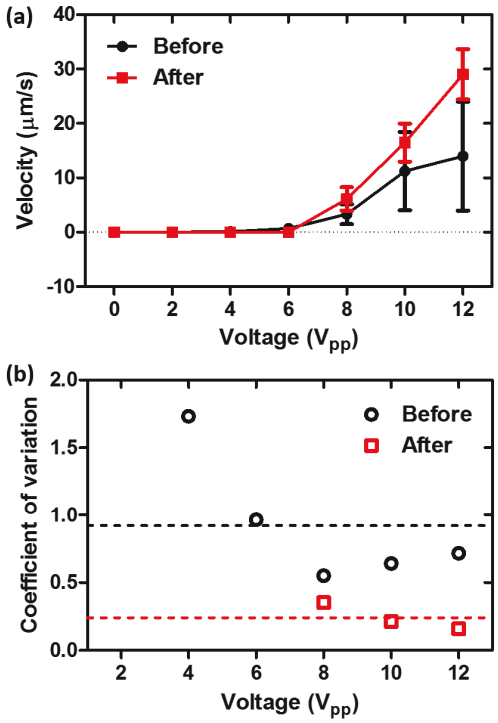

Figure A.9: Effect of direct current-induced breakdown of residual carbon on the performance and the reproducibility of carbon-based AC electroosmotic micropumps: (a) fluid velocities for an AC signal ranging from 0 to 12 V_{PP} at 1 kHz, before and after the DC treatment. Mean *pm* s.d. was plotted. Number of devices, n = 4. (b) The coefficient of variation (CV) for the tested devices before and after DC treatment. The mean CVs were indicated with dotted lines.

by the local film thickness and the location of the highest amorphous carbon concentration.

Regardless the initial resistance values, we were able to obtain open circuits with the low-bias treatment to the carbon IDEAs. The electrodes, which were designed to induce ACEO flow, show significantly enhanced performance and higher reproducibility after breakdown of carbon residues. However, even DC-treated devices still exhibited small variations (mean CV = 0.24) in fluid velocity tests. These small device-to-device variations might be caused by residual carbon that could not be completely removed across the electrodes gap. The remaining material serves as an extension to the electrodes, thus affecting the effective EW/EN ratio and gaps between the electrodes of the micropumps, since the electrode width increases and the gaps decreases. We believe that this easyto-implement method for breaking down residual carbon can be widely applicable to other carbon electronic circuits with small feature sizes, which are currently used for a wide variety of applications.

References

[1] Y. Kuboki, S. Matsusaka, S. Minowa, H. Shibata, M. Suenaga, E. Shinozaki, N. Mizunuma, M. Ueno, T. Yamaguchi, and K. Hatake, "Circulating tumor cell (ctc) count and epithelial growth factor receptor expression on ctcs as biomarkers for cetuximab efficacy in advanced colorectal cancer," *Anticancer Research*, vol. 33, no. 9, pp. 3905–3910, 2013.

[2] C. H. Ahn, J. W. Choi, G. Beaucage, J. H. Nevin, J. B. Lee, A. Puntambekar, and J. Y. Lee, "Disposable smart lab on a chip for point-of-care clinical diagnostics," *Proceedings of the Ieee*, vol. 92, no. 1, pp. 154–173, 2004.

[3] L. Krejcova, L. Nejdl, M. A. M. Rodrigo, M. Zurek, M. Matousek, D. Hynek, O. Zitka, P. Kopel, V. Adam, and R. Kizek, "3d printed chip for electrochemical detection of influenza virus labeled with cds quantum dots," *Biosensors & Bioelectronics*, vol. 54, pp. 421–427, 2014.

[4] Y. Tao, A. Rotem, H. D. Zhang, C. B. Chang, A. Basu, A. O. Kolawole, S. A. Koehler, Y. K. Ren, J. S. Lin, J. M. Pipas, A. B. Feldman, C. E. Wobus, and D. A. Weitz, "Rapid, targeted and culture-free viral infectivity assay in drop-based microfluidics," *Lab on a Chip*, vol. 15, no. 19, pp. 3934–3940, 2015.

[5] J. E. Allen, B. S. Saroya, M. Kunkel, D. T. Dicker, A. Das, K. L. Peters, J. Joudeh, J. J. Zhu, and W. S. El-Deiry, "Apoptotic circulating tumor cells (ctcs) in the peripheral blood of metastatic colorectal cancer patients are associated with liver metastasis but not ctcs," *Oncotarget*, vol. 5, no. 7, pp. 1753–1760, 2014.

[6] C. D. Chin, T. Laksanasopin, Y. K. Cheung, D. Steinmiller, V. Linder, H. Parsa, J. Wang, H. Moore, R. Rouse, G. Umviligihozo, E. Karita, L. Mwambarangwe, S. L. Braunstein, J. van de Wijgert, R. Sahabo, J. E. Justman, W. El-Sadr, and S. K. Sia, "Microfluidics-based diagnostics of infectious diseases in the developing world," *Nature Medicine*, vol. 17, no. 8, pp. 1015–U138, 2011.

[7] W. Jung, J. Han, J.-W. Choi, and C. H. Ahn, "Point-of-care testing (poct) diagnostic systems using microfluidic lab-on-a-chip technologies," *Microelectronic Engineering*, vol. 132, pp. 46–57, 2015.

[8] S. Sharma, J. Zapatero-Rodriguez, P. Estrela, and R. O'Kennedy, "Point-of-care diagnostics in low resource settings: Present status and future role of microfluidics," *Biosensors (Basel)*, vol. 5, no. 3, pp. 577–601, 2015.

[9] G. M. Whitesides, "The origins and the future of microfluidics," *Nature*, vol. 442, no. 7101, pp. 368–373, 2006. 067CI Times Cited:2056 Cited References Count:65.

[10] H. A. Stone, A. D. Stroock, and A. Ajdari, "Engineering flows in small devices: Microfluidics toward a lab-on-a-chip," *Annual Review of Fluid Mechanics*, vol. 36, pp. 381–411, 2004. 775LT Times Cited:1351 Cited References Count:150.

[11] B. J. Kirby, *Micro-and nanoscale fluid mechanics: transport in microfluidic devices*. Cambridge University Press, 2010.

[12] P. Tabeling, *Introduction to Microfluidics*. Oxford University Press, 2005.

[13] N. Graber, H. Ludi, and H. M. Widmer, "The use of chemical sensors in industry," *Sensors and Actuators B-Chemical*, vol. 1, no. 1-6, pp. 239–243, 1990.

[14] A. Nisar, N. AftuIpurkar, B. Mahaisavariya, and A. Tuantranont, "Mems-based micropumps in drug delivery and biomedical applications," *Sensors and Actuators B-Chemical*, vol. 130, no. 2, pp. 917–942, 2008.

[15] X. Hou, Y. S. Zhang, G. T.-d. Santiago, M. M. Alvarez, J. Ribas, S. J. Jonas, P. S. Weiss, A. M. Andrews, J. Aizenberg, and A. Khademhosseini, "Interplay between materials and microfluidics," *Nature Reviews Materials*, vol. 2, no. 5, p. 17016, 2017.

[16] T. Datta-Chaudhuri, E. Smela, and P. A. Abshire, "System-on-chip considerations for heterogeneous integration of cmos and fluidic bio-interfaces," *Ieee Transactions on Biomedical Circuits and Systems*, vol. 10, no. 6, pp. 1129–1142, 2016.

[17] K. Zhu, R. Dietrich, A. Didier, D. Doyscher, and E. Martlbauer, "Recent developments in antibody-based assays for the detection of bacterial toxins," *Toxins*, vol. 6, no. 4, pp. 1325–1348, 2014.

[18] D. J. Laser and J. G. Santiago, "A review of micropumps," *Journal of Micromechanics and Microengineering*, vol. 14, no. 6, pp. R35–R64, 2004.

[19] J. H. Ni, B. Wang, S. Chang, and Q. Lin, "An integrated planar magnetic micropump," *Microelectronic Engineering*, vol. 117, pp. 35–40, 2014.

[20] D. H. Yoon, H. Sato, A. Nakahara, T. Sekiguchi, S. Konishi, and S. Shoji, "Development of an electrohydrodynamic ion-drag micropump using three-dimensional carbon micromesh electrodes," *Journal of Micromechanics and Microengineering*, vol. 24, no. 9, 2014.

[21] H. Mushfique, J. Leach, R. di Leonardo, M. Padgett, and J. Cooper, "An optically driven pump for microfluidics," *Optical Trapping and Optical Micromanipulation Iii*, vol. 6326, 2006.

[22] M. B. Dentry, J. R. Friend, and L. Y. Yeo, "Continuous flow actuation between external reservoirs in small-scale devices driven by surface acoustic waves," *Lab on a Chip*, vol. 14, no. 4, pp. 750–758, 2014.

[23] Z. Cheng, X. D. Wu, J. Cheng, and P. Liu, "Microfluidic fluorescence-activated cell sorting (mu facs) chip with integrated piezoelectric actuators for low-cost mammalian cell enrichment," *Microfluidics and Nanofluidics*, vol. 21, no. 1, 2017.

[24] W. Inman, K. Domansky, J. Serdy, B. Owens, D. Trumper, and L. G. Griffith, "Design, modeling and fabrication of a constant flow pneumatic micropump," *Journal of Micromechanics and Microengineering*, vol. 17, no. 5, pp. 891–899, 2007.

[25] A. Machauf, Y. Nemirovsky, and U. Dinnar, "A membrane micropump electrostatically actuated across the working fluid," *Journal of Micromechanics and Microengineering*, vol. 15, no. 12, pp. 2309–2316, 2005.

[26] Z. J. Jiao, N. T. Nguyen, X. Y. Huang, and Y. Z. Ang, "Reciprocating thermocapillary plug motion in an externally heated capillary," *Microfluidics and Nanofluidics*, vol. 3, no. 1, pp. 39–46, 2007.

[27] H. Abe, Y. Imai, N. Tokunaga, Y. Yamashita, and Y. Sasaki, "Highly efficient electrohydrodynamic pumping: Molecular isomer effect of dielectric liquids, and surface states of electrodes," *Acs Applied Materials & Interfaces*, vol. 7, no. 44, pp. 24492–24500, 2015.

[28] T. S. Gregory, R. Cheng, G. Y. Tang, L. D. Mao, and Z. T. H. Tse, "The magnetohydrodynamic effect and its associated material designs for biomedical applications: A state-of-the-art review," *Advanced Functional Materials*, vol. 26, no. 22, pp. 3942–3952, 2016.

[29] N. Islam and D. Askari, "Performance improvement of an ac electroosmotic micropump by hydrophobic surface modification," *Microfluidics and Nanofluidics*, vol. 14, no. 3-4, pp. 627–635, 2013.

[30] M. Gao and L. Gui, "A handy liquid metal based electroosmotic flow pump," *Lab on a Chip*, vol. 14, no. 11, pp. 1866–1872, 2014. Ah2bj Times Cited:0 Cited References Count:45.

[31] J. Seyed-Yagoobi, "Electrohydrodynamic pumping of dielectric liquids," *Journal of Electrostatics*, vol. 63, no. 6-10, pp. 861–869, 2005.

[32] A. V. Lemoff and A. P. Lee, "An ac magnetohydrodynamic micropump," *Sensors and Actuators B-Chemical*, vol. 63, no. 3, pp. 178–185, 2000.

[33] P. Mitchell, "Microfluidics–downsizing large-scale biology," *Nat Biotechnol*, vol. 19, no. 8, pp. 717–21, 2001.

[34] C.-Y. Lee, G.-B. Lee, J.-L. Lin, F.-C. Huang, and C.-S. Liao, "Integrated microfluidic systems for cell lysis, mixing/pumping and dna amplification," *Journal of Micromechanics and Microengineering*, vol. 15, no. 6, pp. 1215–1223, 2005.

[35] V. H. Perez-Gonzalez, V. Ho, M. Vazquez-Pinon, S. O. Martinez-Chapa, and L. Kulinsky, "A novel micro/nano fabrication process based on the combined use of dielectrophoresis, electroosmotic flow, and electrodeposition for surface patterning," *Journal of Micromechanics and Microengineering*, vol. 25, no. 11, 2015.

[36] I. F. Cheng, H. L. Yang, C. C. Chung, and H. C. Chang, "A rapid electrochemical biosensor based on an ac electrokinetics enhanced immuno-reaction," *Analyst*, vol. 138, no. 16, pp. 4656–4662, 2013.

[37] M. R. Bown and C. D. Meinhart, "Ac electroosmotic flow in a dna concentrator," *Microfluidics and Nanofluidics*, vol. 2, no. 6, pp. 513–523, 2006.

[38] E. M. Melvin, B. R. Moore, K. H. Gilchrist, S. Grego, and O. D. Velev, "On-chip collection of particles and cells by ac electroosmotic pumping and dielectrophoresis using asymmetric microelectrodes," *Biomicrofluidics*, vol. 5, no. 3, 2011.

[39] A. Ramos, H. Morgan, N. G. Green, and A. Castellanos, "Ac electric-field-induced fluid flow in microelectrodes," *Journal of Colloid and Interface Science*, vol. 217, no. 2, pp. 420–422, 1999. 239VG Times Cited:253 Cited References Count:10.

[40] A. Doll, M. Heinrichs, F. Goldschmidtboeing, H. J. Schrag, U. T. Hopt, and P. Woias, "A high performance bidirectional micropump for a novel artificial sphincter system," *Sensors and Actuators a-Physical*, vol. 130, pp. 445–453, 2006.

[41] A. Fadl, S. Demming, Z. Q. Zhang, S. Buttgenbach, M. Krafczyk, and D. M. L. Meyer, "A multifunction and bidirectional valve-less rectification micropump based on bifurcation geometry," *Microfluidics and Nanofluidics*, vol. 9, no. 2-3, pp. 267–280, 2010.

[42] Y. Luo, M. A. Lu, and T. H. Cui, "A polymer-based bidirectional micropump driven by a pzt bimorph," *Microsystem Technologies-Micro-and Nanosystems-Information Storage and Processing Systems*, vol. 17, no. 3, pp. 403–409, 2011.

[43] T. Lemke, G. Biancuzzi, H. Feth, J. Huber, F. Goldschmidtboing, and P. Woias, "Fabrication of normally-closed bidirectional micropumps in silicon-polymer technology featuring photopatternable silicone valve lips," *Sensors and Actuators A: Physical*, vol. 168, no. 1, pp. 213–222, 2011.

[44] H. Feth, F. Pothof, F. Thoma, T. Schmidt, C. Mueller, F. Goldschmidtboeing, and P. Woias, "Design, fabrication and characterization of a piezoelectrically actuated bidirectional polymer micropump," *Microsystem Technologies-Micro-and Nanosystems-Information Storage and Processing Systems*, vol. 20, no. 7, pp. 1299–1310, 2014.

[45] P. S. Chee, R. A. Rahim, R. Arsat, U. Hashim, and P. L. Leow, "Bidirectional flow micropump based on dynamic rectification," *Sensors and Actuators a-Physical*, vol. 204, pp. 107–113, 2013.

[46] I. Lee, P. Hong, C. Cho, B. Lee, K. Chun, and B. Kim, "Four-electrode micropump with peristaltic motion," *Sensors and Actuators a-Physical*, vol. 245, pp. 19–25, 2016.

[47] Y. J. Yang, L. He, C. J. Tang, P. Hu, X. F. Hong, M. Y. Yan, Y. X. Dong, X. C. Tian, Q. L. Wei, and L. Q. Mai, "Improved conductivity and capacitance of interdigital carbon microelectrodes through integration with carbon nanotubes for micro-supercapacitors," *Nano Research*, vol. 9, no. 8, pp. 2510–2519, 2016.

[48] M. Q. A. Rusli, P. S. Chee, R. Arsat, K. X. Lau, and P. L. Leow, "Electromagnetic actuation dual-chamber bidirectional flow micropump," *Sensors and Actuators a-Physical*, vol. 282, pp. 17–27, 2018.

[49] I. Amrani, A. Cheriet, and M. Feliachi, "Design and experimental investigation of a bi-directional valveless electromagnetic micro-pump," *Sensors and Actuators a-Physical*, vol. 272, pp. 310–317, 2018.

[50] M. Vazquez-Pinon, B. Pramanick, F. G. Ortega-Gama, V. H. Perez-Gonzalez, L. Kulinsky, M. J. Madou, H. Hwang, and S. O. Martinez-Chapa, "Hydrodynamic channeling as a controlled flow reversal mechanism for bidirectional ac electroosmotic pumping using glassy carbon microelectrode arrays," *Journal of Micromechanics and Microengineering*, 2019.

[51] U. Barman, A. K. Sen, and S. C. Mishra, "Theoretical and numerical investigations of an electroosmotic flow micropump with interdigitated electrodes," *Microsystem Technologies-Micro-and Nanosystems-Information Storage and Processing Systems*, vol. 20, no. 1, pp. 157–168, 2014.

[52] S. Gassmann, L. Pagel, A. Luque, F. Perdigones, and C. Aracil, "Fabrication of electroosmotic micropump using pcb and su-8," *38th Annual Conference on Ieee Industrial Electronics Society (Iecon 2012)*, pp. 3958–3961, 2012.

[53] H. A. Rouabah, B. Y. Park, R. B. Zaouk, H. Morgan, M. J. Madou, and N. G. Green, "Design and fabrication of an ac-electro-osmosis micropump with 3d high-aspect-ratio electrodes using only su-8," *Journal of Micromechanics and Microengineering*, vol. 21, no. 3, p. 035018, 2011. 726DN Times Cited:3 Cited References Count:31.

[54] J. Wu, "Biased ac electro-osmosis for on-chip bioparticle processing," *Ieee Transactions on Nanotechnology*, vol. 5, no. 2, pp. 84–89, 2006.

[55] W. Wang, C. Y. Gu, K. B. Lynch, J. J. Lu, Z. Y. Zhang, Q. S. Pu, and S. R. Liu, "High-pressure open-channel on-chip electroosmotic pump for nanoflow high performance liquid chromatography," *Analytical Chemistry*, vol. 86, no. 4, pp. 1958–1964, 2014.

[56] A. Mardegan, R. Kamath, S. Sharma, P. Scopece, P. Ugo, and M. Madou, "Optimization of carbon electrodes derived from epoxy-based photoresist," *Journal of the Electrochemical Society*, vol. 160, no. 8, pp. B132–B137, 2013. 223MP Times Cited:2 Cited References Count:45.

[57] B. Pramanick, M. Vazquez-Pinon, A. Torres-Castro, S. O. Martinez-Chapa, and M. Madou, "Effect of pyrolysis process parameters on electrical, physical, chemical and electro-chemical properties of su-8-derived carbon structures fabricated using the c-mems process," *Materials Today-Proceedings*, vol. 5, no. 3, pp. 9669–9682, 2018.

[58] M. Vazquez Pinon, B. Cardenas Benitez, B. Pramanick, V. H. Perez-Gonzalez, M. J. Madou, S. O. Martinez-Chapa, and H. Hwang, "Direct current-induced breakdown to enhance reproducibility and performance of carbon-based interdigitated electrode arrays for ac electroosmotic micropumps," *Sensors and Actuators A: Physical*, vol. 262, pp. 10–17, 2017.

[59] Y. Song, R. Agrawal, and C. L. Wang, "C-mems for bio-sensing applications," *Energy Harvesting and Storage: Materials, Devices, and Applications Vi*, vol. 9493, 2015.

[60] D. Kim, B. Pramanick, A. Salazar, I.-W. Tcho, M. J. Madou, E. S. Jung, Y.-K. Choi, and H. Hwang, "3d carbon electrode based triboelectric nanogenerator," *Advanced Materials Technologies*, pp. 1600160–n/a, 2016.

[61] P. Garcia-Sanchez, A. Ramos, N. G. Green, and H. Morgan, "Experiments on ac electrokinetic pumping of liquids using arrays of microelectrodes," *Ieee Transactions on Dielectrics and Electrical Insulation*, vol. 13, no. 3, pp. 670–677, 2006.

[62] W. Shin, J. M. Lee, R. K. Nagarale, S. J. Shin, and A. Heller, "A miniature, nongassing electroosmotic pump operating at 0.5 v," *Journal of the American Chemical Society*, vol. 133, no. 8, pp. 2374–2377, 2011.

[63] A. Ramos, A. Gonzalez, A. Castellanos, N. G. Green, and H. Morgan, "Pumping of liquids with ac voltages applied to asymmetric pairs of microelectrodes," *Phys Rev E Stat Nonlin Soft Matter Phys*, vol. 67, no. 5 Pt 2, p. 056302, 2003.

[64] M. Pribyl, P. Cervenka, J. Hrdlicka, and D. Snita, "Non-equilibrium modeling of ac electroosmosis in microfluidic channels - parametrical studies," *International Journal of Plasma Environmental Science and Technology*, 2009.

[65] J. Hrdlicka, P. Cervenka, M. Pribyl, and D. Snita, "Mathematical modeling of ac electroosmosis in microfluidic and nanofluidic chips using equilibrium and non-equilibrium approaches," *Journal of Applied Electrochemistry*, vol. 40, no. 5, pp. 967–980, 2009.

[66] D. Kim, A. Raj, L. Zhu, R. I. Masel, and M. A. Shannon, "Non-equilibrium electrokinetic micro/nano fluidic mixer," *Lab Chip*, vol. 8, no. 4, pp. 625–8, 2008.

[67] J. Strong, C. M. Washburn, R. Williams, J. McBrayer, T. Rohwer, R. Stinnett, P. Finnegan, B. Hance, D. Greth, and D. R. Wheeler, "Carbon mems accelerometer," *Proceedings of the 2011 COMSOL Conference, Boston*, 2011.

[68] M. Madou, A. Lal, G. Schmidt, X. Song, K. Kinoshita, M. Fendorf, A. Zettl, and R. White, "Carbon micromachining (c-mems)," *Proceedings of the Symposium on Chemical and Biological Sensors and Analytical Electrochemical Methods*, vol. 97, no. 19, pp. 61–69, 1997. Bj30v Times Cited:8 Cited References Count:0 Electrochemical Society Series.

[69] O. J. A. Schueller, S. T. Brittain, C. Marzolin, and G. M. Whitesides, "Fabrication and characterization of glassy carbon mems," *Chemistry of Materials*, vol. 9, no. 6, pp. 1399–1406, 1997. Xe922 Times Cited:43 Cited References Count:33.

[70] M. J. Madou, *Fundamentals of microfabrication: the science of miniaturization*. CRC press, 2002.

[71] Y. Xia and G. M. Whitesides, "Soft lithography," *Annual Review of Materials Science*, vol. 28, no. 1, pp. 153–184, 1998.

[72] M. Chu, T. T. Nguyen, E. K. Lee, J. L. Morival, and M. Khine, "Plasma free reversible and irreversible microfluidic bonding," *Lab Chip*, 2016.

[73] F. Tuinstra and J. L. Koenig, "Raman spectrum of graphite," *The Journal of Chemical Physics*, vol. 53, no. 3, pp. 1126–1130, 1970.

[74] O. A. Maslova, M. R. Ammar, G. Guimbretiere, J. N. Rouzaud, and P. Simon, "Determination of crystallite size in polished graphitized carbon by raman spectroscopy," *Physical Review B*, vol. 86, no. 13, 2012.

[75] A. Gonzalez, A. Ramos, N. G. Green, A. Castellanos, and H. Morgan, "Fluid flow induced by nonuniform ac electric fields in electrolytes on microelectrodes. ii. a linear double-layer analysis," *Phys Rev E Stat Phys Plasmas Fluids Relat Interdiscip Topics*, vol. 61, no. 4 Pt B, pp. 4019–28, 2000.

[76] A. Ajdari, "Pumping liquids using asymmetric electrode arrays," *Physical Review E*, vol. 61, no. 1, pp. R45–R48, 2000.

[77] Y. K. Ren, W. Y. Liu, Z. J. Wang, and Y. Tao, "Induced-charge electrokinetics in rotating electric fields: A linear asymptotic analysis," *Physics of Fluids*, vol. 30, no. 6, 2018.

[78] R. R. Kamath and M. J. Madou, "Selective detection of dopamine against ascorbic acid interference using 3d carbon interdigitated electrode arrays," *Carbon Electronics: Interfaces to Metals, Dielectrics, and Electrolytes*, vol. 61, no. 7, pp. 65–73, 2014.

[79] Y. Lim, J. I. Heo, M. Madou, and H. Shin, "Monolithic carbon structures including suspended single nanowires and nanomeshes as a sensor platform," *Nanoscale Res Lett*, vol. 8, no. 1, p. 492, 2013.

[80] G. Canton, T. Do, L. Kulinsky, and M. Madou, "Improved conductivity of suspended carbon fibers through integration of c-mems and electro-mechanical spinning technologies," *Carbon*, vol. 71, pp. 338–342, 2014.

[81] M. Kurek, F. K. Larsen, P. E. Larsen, S. Schmid, A. Boisen, and S. S. Keller, "Nanomechanical pyrolytic carbon resonators: Novel fabrication method and characterization of mechanical properties," *Sensors*, vol. 16, no. 7, p. 1097, 2016.

[82] B. Hsia, M. S. Kim, M. Vincent, C. Carraro, and R. Maboudian, "Photoresist-derived porous carbon for on-chip micro-supercapacitors," *Carbon*, vol. 57, pp. 395–400, 2013.

[83] X. Y. Xiao, T. E. Beechem, M. T. Brumbach, T. N. Lambert, D. J. Davis, J. R. Michael, C. M. Washburn, J. Wang, S. M. Brozik, D. R. Wheeler, D. B. Burckel, and R. Polsky, "Lithographically defined three-dimensional graphene structures," *Acs Nano*, vol. 6, no. 4, pp. 3573–3579, 2012.

[84] H. Xu, K. Malladi, C. Wang, L. Kulinsky, M. Song, and M. Madou, "Carbon post-microarrays for glucose sensors," *Biosens Bioelectron*, vol. 23, no. 11, pp. 1637–44, 2008.

[85] Y. L. Zhang, P. C. Gu, and X. Q. Fan, "Progress on research of mems-based micropump," *ICEPT: 2006 7th International Conference on Electronics Packaging Technology, Proceedings*, pp. 527–532, 2006.

[86] R. Martinez-Duarte, P. Renaud, and M. J. Madou, "A novel approach to dielectrophoresis using carbon electrodes," *Electrophoresis*, vol. 32, no. 17, pp. 2385–92, 2011.

[87] R. Martinez-Duarte, r. Gorkin, R. A., K. Abi-Samra, and M. J. Madou, "The integration of 3d carbon-electrode dielectrophoresis on a cd-like centrifugal microfluidic platform," *Lab Chip*, vol. 10, no. 8, pp. 1030–43, 2010.

[88] S.-H. Huang, S.-K. Wang, H. S. Khoo, and F.-G. Tseng, "Ac electroosmotic generated in-plane microvortices for stationary or continuous fluid mixing," *Sensors and Actuators B: Chemical*, vol. 125, no. 1, pp. 326–336, 2007.

[89] K. F. Hoettges, M. B. McDonnell, and M. P. Hughes, "Continuous flow nanoparticle concentration using alternating current-electroosmotic flow," *Electrophoresis*, vol. 35, no. 4, pp. 467–473, 2014.

[90] R. Hart, R. Lec, and H. Noh, "Enhancement of heterogeneous immunoassays using ac electroosmosis," *Sensors and Actuators B-Chemical*, vol. 147, no. 1, pp. 366–375, 2010.

[91] G. T. Teixidor, R. A. Gorkin, P. P. Tripathi, G. S. Bisht, M. Kulkarni, T. K. Maiti, T. K. Battacharyya, J. R. Subramaniam, A. Sharma, B. Y. Park, and M. Madou, "Carbon microelectromechanical systems as a substratum for cell growth," *Biomedical Materials*, vol. 3, no. 3, 2008.

[92] S. L. Jiang, T. L. Shi, X. B. Zhan, S. Xi, H. Long, B. Gong, J. J. Li, S. Y. Cheng, Y. Y. Huang, and Z. R. Tang, "Scalable fabrication of carbon-based mems/nems and their applications: a review," *Journal of Micromechanics and Microengineering*, vol. 25, no. 11, 2015.

[93] M. Madou, V. Perez-Gonzalez, and B. Pramanick, *Carbon: The Next Silicon?: Book 2–Applications*. Momentum Press, 2016.

[94] K. Molhave, S. B. Gudnason, A. T. Pedersen, C. H. Clausen, A. Horsewell, and P. Boggild, "Transmission electron microscopy study of individual carbon nanotube breakdown caused by joule heating in air," *Nano Letters*, vol. 6, no. 8, pp. 1663–1668, 2006.

[95] R. Murali, Y. X. Yang, K. Brenner, T. Beck, and J. D. Meindl, "Breakdown current density of graphene nanoribbons," *Applied Physics Letters*, vol. 94, no. 24, 2009.

[96] H. Kitsuki, T. Yamada, D. Fabris, J. R. Jameson, P. Wilhite, M. Suzuki, and C. Y. Yang, "Length dependence of current-induced breakdown in carbon nanofiber interconnects," *Applied Physics Letters*, vol. 92, no. 17, 2008.

[97] S. Frank, P. Poncharal, Z. L. Wang, and W. A. Heer, "Carbon nanotube quantum resistors," *Science*, vol. 280, no. 5370, pp. 1744–6, 1998.

[98] P. C. Collins, M. S. Arnold, and P. Avouris, "Engineering carbon nanotubes and nanotube circuits using electrical breakdown," *Science*, vol. 292, no. 5517, pp. 706–709, 2001.

[99] H. O. Pierson, *Handbook of carbon, graphite, diamonds and fullerenes: processing, properties and applications*. William Andrew, 2012.

[100] O. J. Schueller, S. T. Brittain, and G. M. Whitesides, "Fabrication of glassy carbon microstructures by soft lithography," *Sensors and Actuators A: Physical*, vol. 72, no. 2, pp. 125–139, 1999.

[101] M. Balat-Pichelin, J. Robert, and J. Sans, "Emissivity measurements on carbon-carbon composites at high temperature under high vacuum," *Applied Surface Science*, vol. 253, no. 2, pp. 778–783, 2006.

[102] P. G. T. Howell, K. M. W. Davy, and A. Boyde, "Mean atomic number and backscattered electron coefficient calculations for some materials with low mean atomic number," *Scanning*, vol. 20, no. 1, pp. 35–40, 1998.

[103] L. Amato, A. Heiskanen, R. Hansen, L. Gammelgaard, T. Rindzevicius, M. Tenje, J. Emneus, and S. S. Keller, "Dense high-aspect ratio 3d carbon pillars on interdigitated microelectrode arrays," *Carbon*, vol. 94, pp. 792–803, 2015.

[104] Y. A. Levendis and R. C. Flagan, "Combustion of uniformly sized glassy-carbon particles," *Combustion Science and Technology*, vol. 53, no. 2-3, pp. 117–136, 1987.

[105] K.-J. Lee, A. P. Chandrakasan, and J. Kong, "Breakdown current density of cvd-grown multilayer graphene interconnects," *Electron Device Letters, IEEE*, vol. 32, no. 4, pp. 557–559, 2011.

[106] A. A. Balandin, "Thermal properties of graphene and nanostructured carbon materials," *Nature materials*, vol. 10, no. 8, pp. 569–581, 2011.